Chemical Science

ROYAL SOCIETY OF CHEMISTRY

REVIEW

View Article Online
View Journal | View Issue

Check for updates

Cite this: *Chem. Sci.*, 2021, **12**, 71

Local probe investigation of electrocatalytic activity

N. Limani, A. Boudet, N. Blanchard, B. Jousselme and R. Cornut *

As the world energy crisis remains a long-term challenge, development and access to renewable energy sources are crucial for a sustainable modern society. Electrochemical energy conversion devices are a promising option for green energy supply, although the challenge associated with electrocatalysis have caused increasing complexity in the materials and systems, demanding further research and insights. In this field, scanning probe microscopy (SPM) represents a specific source of knowledge and understanding. Thus, our aim is to present recent findings on electrocatalysts for electrolysers and fuel cells, acquired mainly through scanning electrochemical microscopy (SECM) and other related scanning probe techniques. This review begins with an introduction to the principles of several SPM techniques and then proceeds to the research done on various energy-related reactions, by emphasizing the progress on non-noble electrocatalytic materials.

Received 6th August 2020
Accepted 4th November 2020

DOI: 10.1039/d0sc04319b

rsc.li/chemical-science

Open Access Article. Published on 19 November 2020. Downloaded on 4/20/2026 1:55:05 AM.
This article is licensed under a Creative Commons Attribution-NonCommercial 3.0 Unported Licence.

Introduction

In a time when our planet is suffering from environmental disasters caused by fossil fuel pollution, which put at risk the health of humankind,[1,2] it is of primary importance to have renewable energy accessible worldwide.[3] Among other environmentally friendly energy providers,[4] fuel cells are green-energy conversion devices that convert chemical energy to electrical energy by oxidizing a fuel in the anode and reducing another chemical species at the cathode.[5] Some of the fuels that can be utilized are formic acid,[6] hydrogen sulfide,[7] hydrazine,[8] ethanol,[9] methanol,[10] ammonia[11] and hydrogen.[12] The latter is considered as one of the most unique fuels:[13–16] besides several methodologies for hydrogen generation,[17] an electrolyser is a device where H_2 can be produced from water at the cathode, while O_2 evolves at the anode.[18] In a regenerative fuel cell, H_2 and O_2 are generated while the device functions in the electrolytic mode, and then these products are fed to the fuel cell in order to produce electricity by operating in the galvanic mode (Fig. 1).[19]

However, all these reactions require electrocatalysts that are based on noble metals, such as Pt-based materials for the oxygen reduction reaction (ORR), hydrogen oxidation reaction (HOR) and hydrogen evolution reaction (HER),[20,21] along with IrO_2 and RuO_2 for the oxygen evolution reaction (OER) in acidic media electrolysers.[22,23] This is one of the factors leading to

Université Paris-Saclay, CEA, CNRS, NIMBE, LICSEN, Gif-sur-Yvette, 91191, France. E-mail: renaud.cornut@cea.fr

Ndrina Limani received her BSc degree in Chemical Engineering from the University of Prishtina (2017) in Kosovo, after which she continued her master's studies abroad with a fully funded Erasmus+ scholarship. She earned a double MSc degree in Chemistry from the University of Porto in Portugal and Paris-Saclay University in France (2019). Presently, she is conducting her PhD studies as a Marie Curie Early-Stage-Researcher (SENTINEL-ITN) in the field of SECM and electrocatalysis at CEA-Saclay, under the supervision of Dr Renaud Cornut and Dr Bruno Jousselme.

Alice Boudet graduated in 2018 from the engineering school Grenoble INP-Phelma with a degree in electrochemistry and process engineering. She is now pursuing a PhD at Université Paris-Saclay in the laboratory LICSEN from CEA Saclay. She is working under the supervision of Dr Bruno Jousselme and Dr Renaud Cornut on SECM for the evaluation of the catalytic activity of PGM-free catalysts. Her work involves both experimental and modelling studies.

© 2021 The Author(s). Published by the Royal Society of Chemistry

Open Access Article. Published on 19 November 2020. Downloaded on 4/20/2026 1:55:05 AM.
This article is licensed under a Creative Commons Attribution-NonCommercial 3.0 Unported Licence.

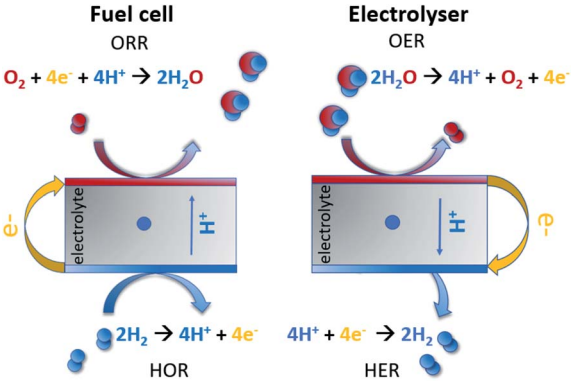

Fig. 1 Fuel cell and electrolyser reaction scheme in acidic media.

a stagnation in fuel cell commercialization,[24,25] which is motivating researchers to seek methods to study these reactions and alternative non-scarce and simpler electrocatalysts.[26,27]

Here, we review the work that has been done in recent 5 years by employing scanning probe electrochemical microscopy for studying electrocatalysts, with an emphasis on SECM as the most used method in this field within the scanning probe techniques. Initially, the working principle of the methods will be presented. Then, some recent studies of noble-metal-based electrocatalysts for the ORR, OER and HER are mentioned; however we emphasize the major trend of the field, *i.e.* the developments in non-noble materials and the experimental conditions used. Finally, some emerging SECM applications in electrocatalysis, namely in the hydrogen oxidation reaction (HOR) and carbon dioxide reduction reaction (CO_2RR), will be presented briefly. To the best of our knowledge, similar treatment of this topic is not present in the literature since the reviews of Bertoncello[28] and Polcari[29] published in 2010 and 2016 respectively. Until now, a wide range of novel electroactive materials and ideas have emerged and will be discussed herein.

Nicolas Blanchard received his BSc degree in Chemistry from the University of Sorbonne (2017) in France and his master's degree in materials chemistry from PSL University (2019). After a short experience at ICMPE in Paris Est on the electrochemical reduction of carbon dioxide, he is currently doing a PhD thesis in electrochemistry under the supervision of Renaud Cornut and Bruno Jousselme at LICSEN from CEA Saclay. His job is to study the transport of species within of fuel cell electrodes, using mainly electrochemical microscopy (SECM) and electrochemical impedance spectroscopy (EIS) techniques.

Bruno Jousselme is a Senior Scientist in the LICSEN group at CEA Saclay LICSEN. Hired in 2006, he started new research programs on the synthesis of conjugated systems and surface functionalization for applications in molecular electronics and renewable energies. His motivations in the latter field are to develop cheap, stable and efficient nanomaterials for photo- and electro-catalysis based mainly on carbon nanotubes.

Rotating disk electrode (RDE) and rotating ring disk electrode (RRDE)

The investigation of electrocatalysts is mostly done through RDE and RRDE methods, based on a three-electrode cell where the working electrode (WE) is typically a disk glassy carbon electrode surrounded by an insulating material. The RRDE WE has an additional ring electrode (generally platinum) separated by GC through the insulating material.[30] This ring electrode serves for the detection of intermediates that may be produced by the sample (often H_2O_2, detailed more in the ORR section) and works independently from GC.[31] The working electrodes are subjected to rotations at certain speeds (convection). The higher the convection, the thinner the diffusion layer close to the electrode, leading to a steady state current.[32] The diffusion within the layer aids the transport of the reactant to the catalyst.[32] Hence, this apparatus is a convenient means for the quantitative study of electrode kinetics.

Scanning probe microscopy (SPM)

SPM techniques are a family of instruments which consist in the displacement of a probe in the vicinity of a substrate, thus providing spatially localized information of different nature, depending on the type of interaction between the probe and the sample. The possibility to use different sizes and materials of probes expands their application possibility in materials science,

Renaud Cornut has been a researcher at LICSEN in CEA Saclay since 2011. He graduated in 2009 from Grenoble INP-Phelma with a degree in electrochemistry and numerical simulation, and did post-doctorate at UQAM 2009–2011 in Bio-SECM and lithium batteries. His current topics of interest are SECM and fuel cell electrochemistry.

© 2021 The Author(s). Published by the Royal Society of Chemistry

Open Access Article. Published on 19 November 2020. Downloaded on 4/20/2026 1:55:05 AM.
This article is licensed under a Creative Commons Attribution-NonCommercial 3.0 Unported Licence.

electrochemistry, biology, biochemistry and medicine. Besides probing a material, SPM can also be helpful for material alteration at the nanoscale, such as the usage of an AFM cantilever probe as a means for nanolithography.[33] Here we will review the principles and application of some electrochemical scanning probe techniques such as SECM, SECM-AFM, SECM-SICM and SECCM in the study of electrocatalysts for fuel cells and electrolyzers.

Scanning electrochemical microscopy (SECM)

As an alternative to RDE and RRDE methods, scanning electrochemical microscopy is a pure diffusion-based technique and a type of scanning probe microscopy which enables the analysis of redox processes in samples by determining their spatially resolved chemical, electrochemical, and/or topographic specificities. This can be acquired by placing an ultramicroelectrode (UME, typically ≤25 μm) at a certain distance from the sample of interest and moving it across the sample (x, y direction), by keeping the UME still (fixed x, y, z), or by moving the UME only in the z direction.[34] The UME is placed along with the sample, counter and reference electrode in a cell and controlled by using a potentiostat (Fig. 2). Electrochemical information is obtained from the (electro)chemical reactions occurring either at the UME, at the sample, or both. The tip-to-sample distance d and tip size have great impact on the spatial resolution.[35] The d can be established by obtaining approach curves,[36] which can then be compared with theory.[37,38]

The microelectrodes commonly used in SECM display different phenomena from macroelectrodes typically used by the RDE method. While in flat macroelectrodes the diffusion of species occurs in a perpendicular manner, in microelectrodes hemispherical diffusion around the electrode occurs, promoting higher mass transfer and limiting current densities[40] owing to the geometry (which can be diverse[41]) and the small size of the UME. In other words, smaller dimensions of the electrode permit a better sensitivity in measurements, and the absence of convection in SECM investigations simplifies the interpretation of results compared to hydrodynamic methods. A

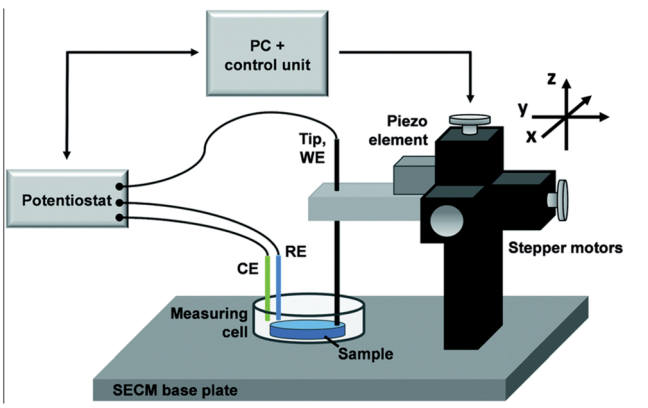

Fig. 2 Illustration of the scanning electrochemical microscope set-up. Reproduced from ref. 39 with permission from the Royal Society of Chemistry, © 2015.

derived equation from Fick's law which expresses the diffusion flux of species is shown in eqn (1),[42] where i represents the current intensity, n the transferred electrons, F the Faraday constant, A the electrode area, D the diffusion coefficient, t is the time, r_0 the radius of UME and the last expression ($4NFDC^*r_0$) represents i_{ss} which is the steady state current intensity.

$$i \approx \frac{nFAD^{0.5}C^*}{\pi^{0.5}t^{0.5}} + 4nFDC^*r_0 \quad (1)$$

As the spatial resolution in SECM depends on the size of the electrode, the usage of nano-sized ones permits electrochemical studies in single nano-objects.[43,44] This offers several opportunities; for example it allows the distinction of activity between different nano-objects in the same catalyst, which can lead to important indications for appropriate design of electroactive materials.[45] Besides, the possibility to perform experiments with small gaps between the catalyst and the tip enables the detection of specifically short-lived intermediates (*i.e.* $CO_2^{\bullet-}$) that can be produced by the sample, paving the way to a better understanding of reaction mechanisms.[46] Localized catalyst fabrication has been performed with SECM,[47] along with the assessment of charge density,[48] dissolution[49] and diffusion[50] of species. SECM lately was used even to determine the location where the OER occurs within the sample[51] or in the formation of a solid electrolyte interphase (SEI) in lithium ion batteries.[52] SECM has also found utility in H_2O_2 detection as the intermediate during the ORR and has some advantages compared to the traditional macroscopic method, RRDE. By using the latter, the amount of H_2O_2 detected at the ring *versus* the one really produced by the sample is ambiguous, since the amount of H_2O_2 close to the disk electrode may vary with the rotation of the electrode.[53] Furthermore, catalyst layers studied with this method are often quite thick, in which case H_2O_2 can decompose within the layer before getting in contact with the ring, leading to lower amounts of intermediates detected.[54] Aside from intermediates, the SECM detection of gases such as oxygen in OER investigations is rigorous. Even though generally the gas-evolving reactions are quite utile in industry, their in-depth electrochemical study with traditional methods can be a challenge considering that there is formation of bubbles, which may often block the electrodes and prevent the accurate measurement of current. The lower current densities under SECM conditions make the appearance of bubbles less of a problem. Moreover, determining the correct onset potential with a RDE may be questionable, since it can include other oxidation reactions that may occur in the catalyst.[55] This can be rectified if the sample is studied by SECM, through measuring the anodic current generated at the electrocatalyst and the cathodic current of the UME, in which the reduction of the previously evolved O_2 occurs.[55,56] Furthermore, for the HER SECM is a convenient way to evaluate the faradaic efficiency of the system. The capability of SECM to map the electrocatalytic activity of a catalyst layer is of great importance, considering that the layers are often not homogeneous. The possibility to perform conductivity measurements[57] with SECM is also an advantage, as it can ease the interpretation of the electrocatalytic activity results. Evidently, there are numerous appealing features of SECM which benefit electrocatalytic studies.

Open Access Article. Published on 19 November 2020. Downloaded on 4/20/2026 1:55:05 AM.
This article is licensed under a Creative Commons Attribution-NonCommercial 3.0 Unported Licence.

However, challenges associated with this technique are noteworthy as well, one of the most important ones being the separate measurement of topography and electrocatalytic activity, in other words the assessment of net electrochemical activity without topographic influences. It has been shown that theoretically these influences cannot be entirely removed.[58] Nevertheless, many successful attempts were made for solving this issue by instrumental manipulations, such as the development of shear-force SECM (SF-SECM),[59] intermittent-contact SECM (IC-SECM),[60] hopping-intermittent-contact SECM (HIC-SECM),[61] alternating-current SECM (AC-SECM),[62] or the combination of SECM with SICM or AFM. When working with conventional SECM with a micro-scale d and tip, the topographic influences become somewhat less important compared to nanoscale measurements. As in any other SPM technique, SECM spatial resolution is mainly governed by the size of the probe used in the experiment, and the most straightforward way to suppress convolution (although sometimes experimentally challenging) is to decrease the size of the probe: moreover, maintaining a constant d is not possible in conventional SECM, limiting the usage of samples to very flat and aligned ones.[63] Another drawback is the fact that the sample and tip have to be immersed in solution during SECM experiments, possibly for hours, which can lead to surface changes in the sample and tip.

Since the introduction of SECM by Bard *et al.* in 1989,[64] a great deal of effort has been made by researchers to improve it and to expand its application possibilities. To name a few, an interesting approach for investigating the reactivity of ion transfer in liquid/membrane and liquid/liquid interfaces by means of SECM was introduced by Shao and Mirkin in 1998.[65] Moreover, the first simultaneous measurements of topography and electrochemistry in a fluid were acquired by Macpherson and Unwin by combining AFM and SECM.[66] Nanoscale measurements were performed as well, for which a detailed guide for nano-electrode fabrication with radii as small as 10 nm was presented by Katemann and Schuhmann.[67] Furthermore, the widely used redox competition mode was developed by Eckhard *et al.*[68] Owing to such advancements in the technique, nowadays the utilization of SECM enables researchers to obtain very useful information on a variety of materials for numerous applications.[44,69–71]

SECM modes

Depending on the purpose of experiment, several modes can be employed by SECM and they are reviewed in more detail by several groups, such as Bard *et al.*[64] and Polcari *et al.*[29] Herein, a rather brief presentation of the modes applied in electrocatalysis will be presented and illustrated (Fig. 3–5). Their application for the respecting reactions will be detailed in the rest of the review.

Feedback mode

Feedback mode is one of the most used ones in the field, described initially along with SECM itself in 1989. Let us consider an oxidized species O as a free mediator present in solution that is reduced to R by a polarized UME. At a large distance from the sample, the tip exhibits a constant diffusion-limited current i_{ss}, whose magnitude is proportional to the concentration of O and electrode size. As illustrated Fig. 4, if the sample is not reactive (an insulator) and the tip approaches it, the hemispherical diffusion will be disturbed and thus the diffusion of O to the tip will be hindered. This will lead to a decrease in the diffusion-limited tip current, known as the negative feedback effect.[42] In the case of positive feedback, an electrochemically active sample (conductor) is approached by the tip. The substrate can thus oxidize the R formed at the tip back to O, thus increasing the concentration of O in the diffusion zone and increasing the tip current.[42] The current *vs.* d curves obtained while the tip approaches a conductive or insulating substrate are called approach curves (Fig. 3). The concentration and diffusion coefficient of O do not influence the approach curve, as it includes dimensionless variables solely.[34] The degree of current change is dictated by the activity of the sample, enabling the distinction between more and less active spots[42] in the same substrate and the determination of d and the electrode radius a. The r_g parameter (insulating part of the UME) has an influence on negative feedback curves as it hampers the diffusion.[34] Through feedback mode one measures the current only at the tip, thus it is convenient to use in cases when the substrate cannot be polarized.

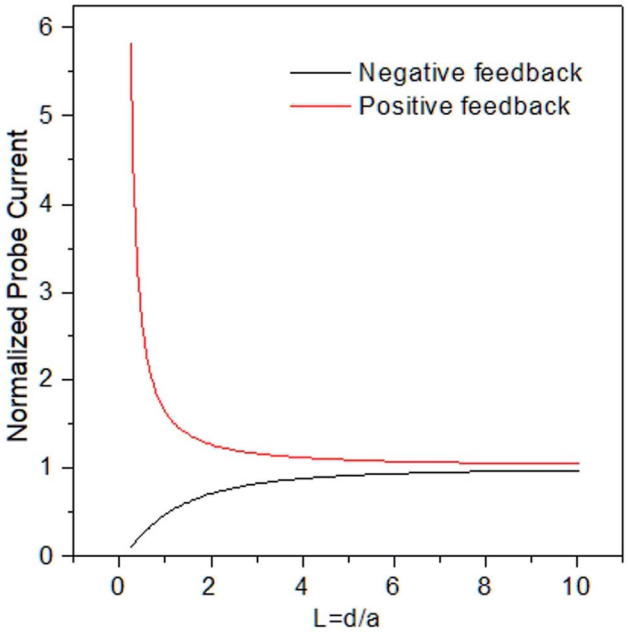

Fig. 3 Illustration of positive and negative feedback approach curves.

Generation/collection (GC) modes

While in feedback mode the redox mediator is already present in solution, which leads to a faradaic background current in the tip,[42] in the generation/collection modes the mediator is produced at one of the electrodes. The generation of redox species at the sample, after which they diffuse to the tip and undergo electrochemical reactions, is known as sample generation/tip collection (SG/TC) mode.[72] In this case, the current of the tip will provide information about the electrochemical

© 2021 The Author(s). Published by the Royal Society of Chemistry

Open Access Article. Published on 19 November 2020. Downloaded on 4/20/2026 1:55:05 AM.
This article is licensed under a Creative Commons Attribution-NonCommercial 3.0 Unported Licence.

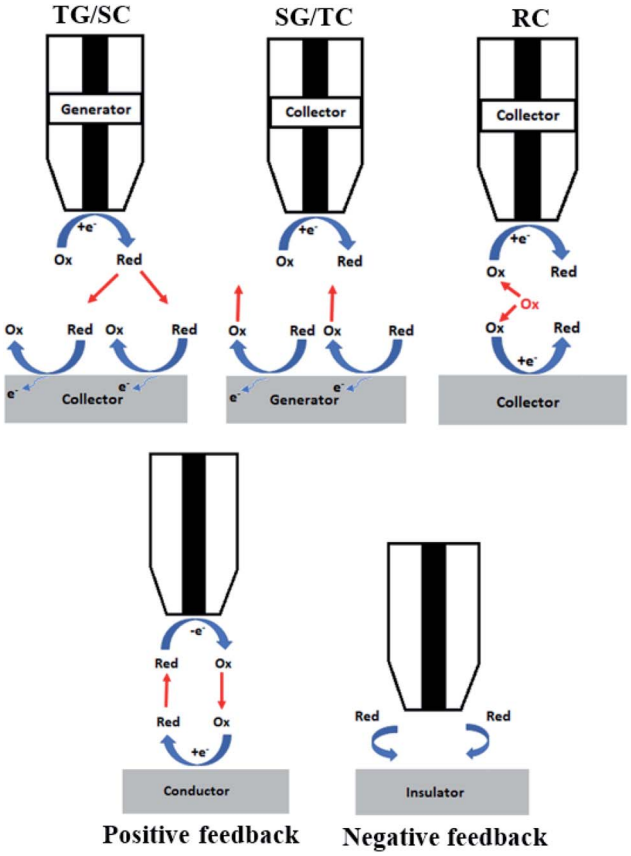

Fig. 4 Schematic representation of the main SECM modes. Substrate generation/tip collection (SG/TC), tip generation/substrate collection (TC/SC), redox competition (RC), and positive and negative feedback modes.

activity of the sample. Conversely, the production of species at the tip and their diffusion in the sample to get oxidized or reduced is known as tip generation/sample collection (TG/SC) mode.[73] Herewith, the sample current holds information about the sample local electrochemical activity at the tip location.[42]

Redox competition (RC) mode

In the Redox Competition (RC) mode,[68] the sample and the tip undergo the same reaction, and they both compete for the same mediator. When the tip approaches the sample in line scans (x, y direction), due to the extensive consumption of the mediator by the sample as well, there is less mediator detected by the tip; hence there is a decrease in the tip current which is measured.[68] The RC mode suppresses the background current issue generally encountered with TG/SC mode.[68]

Surface interrogation mode (SI-SECM)

The SI mode was introduced by Bard's group back in 2008.[74] In contrast to the other modes, it is based on transient measurements. It consists in a titrant generation from a redox mediator through a SECM tip, which then undergoes a chemical reaction with certain species generated at the closely placed substrate. In other words, the generation and collection of the oxidized and

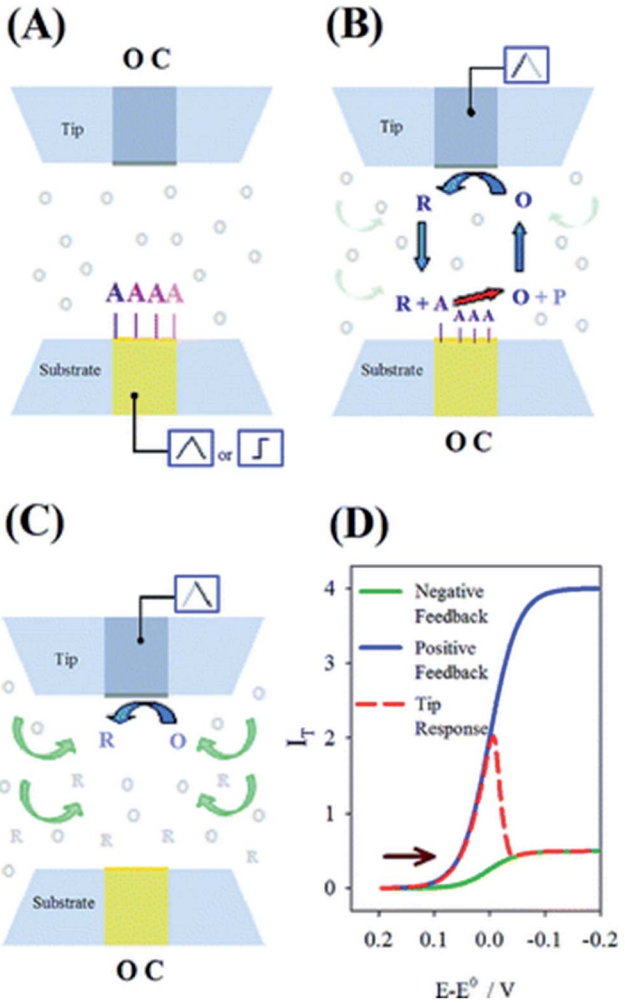

Fig. 5 Schematics of the proposed mechanism for the surface interrogation. (A) A reactive species is chemically or electrochemically adsorbed on the substrate upon a potential scan or step while the tip is at open circuit. (B) The substrate is put to open circuit, and the tip generates the titrant, which reacts at the surface of the substrate to support positive feedback at the same tip. (C) Upon consumption of the adsorbate at the substrate, the tip experiences negative feedback. (D) Expected current response at the tip following the events depicted in panels A–C for an arbitrary electrode setup. Reproduced from ref. 74 with permission from the American Chemical Society © 2008.

reduced mediator species lead to variations in the electrochemical signals, which can be detected by the SECM tip. This leads to a transient positive feedback loop as long as the investigated species is being consumed.[74]

Scanning ion conductance microscopy (SICM)

This technique, introduced by Hansma *et al.*,[75] is typically based on a bias application between a single-channel nanopipette electrode which is filled with an electrolyte and contains a quasi-reference counter electrode (QRCE) inside and in the bulk solution, in which case the ion flow between these electrodes produces an ion current (I) (Fig. 6).[76,77] The flowing ionic current

Open Access Article. Published on 19 November 2020. Downloaded on 4/20/2026 1:55:05 AM.
This article is licensed under a Creative Commons Attribution-NonCommercial 3.0 Unported Licence.

then depends on the nanopipette and electrolyte resistance.[77] By detecting the current flow in the nanopipette with an applied bias, SICM can be a powerful tool for mapping spatial distributions of ionic fluxes. Hereby, the modulation of the probe distance or bias can provide information about topography and activity with a single channel probe, simultaneously.[78] Besides topography measurements, SICM has also found utility in the determination of ion conductivity.[79] Very recently a development has been made, where SICM can be used for generating local electrochemical impedance spectra, in which case the local capacitance and topography can be determined separately in one measurement.[80] It's worth mentioning that the possibility of non-contact imaging with SICM allows the investigation of fragile samples that otherwise are investigated with difficulty by AFM for example.[76] This being said, SICM has been especially useful in studying living systems, their morphology, physiological activity and subcellular structures.[81] The temporal resolution once considered as a challenge has been improved by modulating its mechanical and software elements.[82] SICM application has expanded to electrocatalysis as well thanks to its combination with SECM (SICM-SECM). In this way, one can take advantage of the possibility to record faradaic signals with SECM while at the same time avoiding its inferiority in topographic measurements.[77] In contrast to conventional SECM, the d in SICM can be controlled,[77] although it is only relatively specialized.[83]

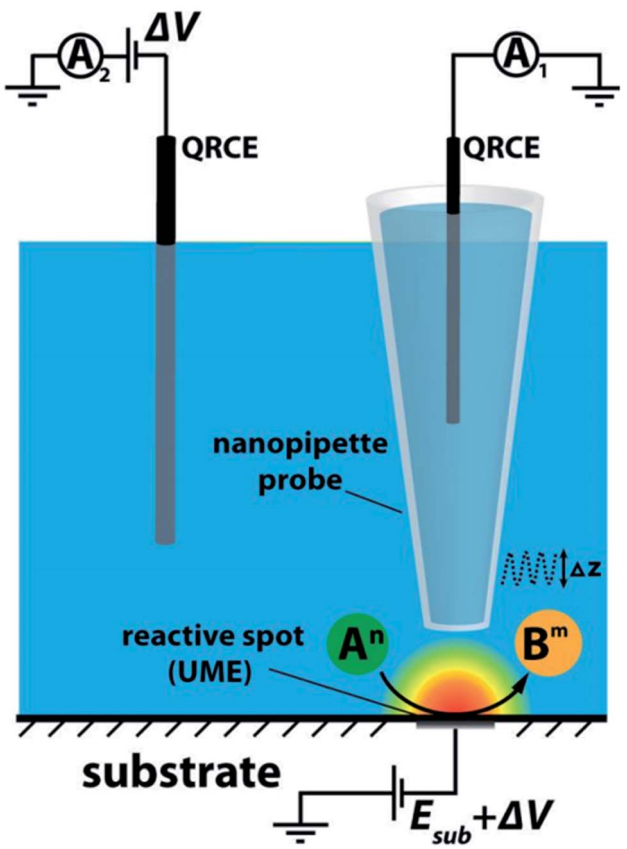

Fig. 6 SICM set-up scheme. Reproduced from ref. 78 with permission from the American Chemical Society © 2016.

Depending on the application, several SICM modes are possible and they are reviewed carefully elsewhere.[76,84]

Scanning electrochemical cell microscopy (SECCM)

Introduced in 2010 by Ebejer *et al.*,[85] SECCM is a technique based on an electrolyte-filled, dual or single-barred pipette, with a QRCE in every channel (Fig. 7).[63] A droplet is formed at the end of the pipette when it is in contact with the sample. Once a potential is applied between the electrodes, ion and electron transfer occurs through the droplet meniscus. This results in modulations of conductance current (i_{dc}) which serves as a feedback signal for probe positioning. The pipette moves laterally across the surface at a certain d or in hopping mode, during which the current signals are recorded.[63] This technique enables the imaging of electrochemistry, conductivity and topography of samples, simultaneously.[86] The fact that only a small part of the sample is in contact with the solution very briefly makes SECCM an encouraging method for investigating samples sensitive to corrosion, passivation or surface fouling.[76] SECCM has been used for performing microscale voltametric measurements, correlating the properties of specific parts of the substrate with the electron-transfer kinetics.[87] Moreover, it has found utility in the fabrication of polymer nanostructures,[88] in assessing localized capacitance,[89] electrochemical activity,[90] and ion transfer[91] and even in nanoparticle landing experiments.[92] One of the important advantages of this method is the reduced time needed for acquiring the images.[93] SECCM is up-and-coming in the electrocatalysis area, as reactive sites can be detected explicitly through local electrochemical and structural analysis. Being introduced recently (in 2010), there is still room for SECCM development compared to analogue techniques.[83] Many features of this method are explained thoroughly elsewhere.[63,94]

Atomic force microscopy (AFM)

AFM, introduced in 1986, is a scanning probe technique which measures attractive or repulsive interactions between a sharp tip on a flexible cantilever and a sample under investigation. After the cantilever approaches the surface, it gets deflected by the interactions with it in accordance with Hooke's law (Fig. 8).[96] This deflection is measured thanks to a laser beam and a photodiode and holds information about the sample,[96] while the sample or the tip are moved by a piezo scanner. There are certain possibilities of AFM operation, such as in contact, noncontact, static or dynamic mode for which a comprehensive introduction was made by Haugstad.[97] This high resolution technique made it possible to image non-conducting samples in open air, something which was not achievable back then by its analogue scanning tunneling microscopy (STM).[98–100] AFM is mostly used for assessing the surface topography, morphology, and roughness. Its application possibilities are excessive, to name a few: molecule generation, manipulation and characterization,[101] study of the mechanical properties of cells,[99] bubble–particle interactions,[102]

© 2021 The Author(s). Published by the Royal Society of Chemistry

Open Access Article. Published on 19 November 2020. Downloaded on 4/20/2026 1:55:05 AM.
This article is licensed under a Creative Commons Attribution-NonCommercial 3.0 Unported Licence.

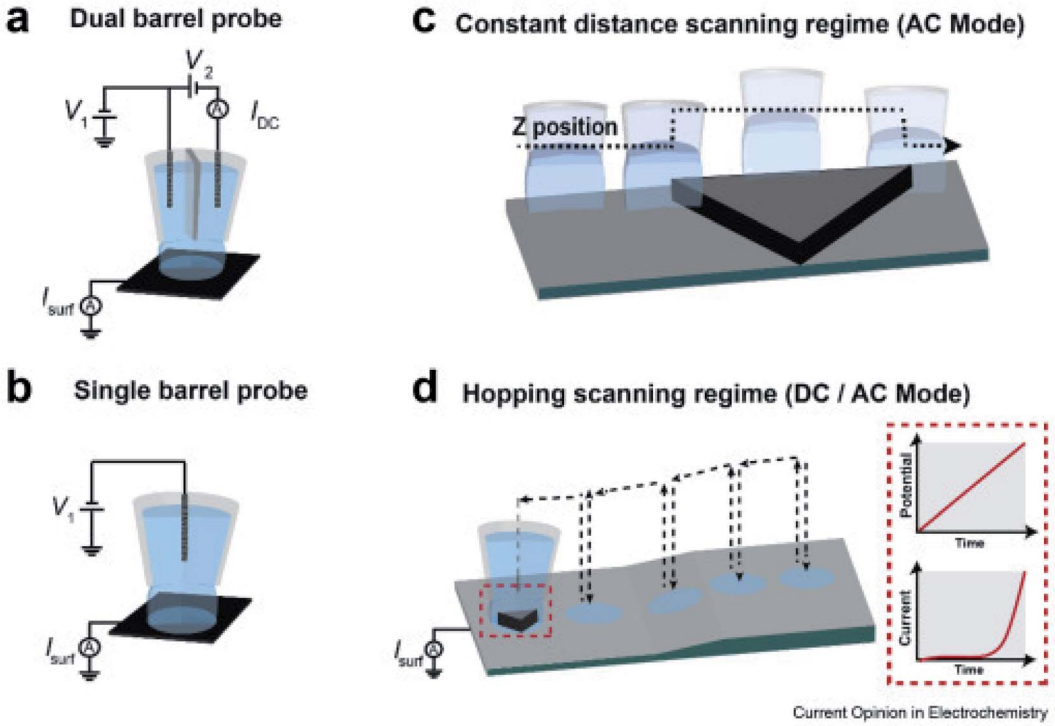

Fig. 7 SECCM schematic set-up for voltammetry and amperometry. (a) dual barrel, (b) single barrel probes (micro- or nano-pipets) filled with an electrolyte and QRCE(s) used as SECCM scanning probes; schematic of probe movement at a (c) constant tip distance from the surface, and (d) hopping scanning regime over the sample. Inset in (d) shows the *E*–*t* linear sweep voltammogram (LSV) and the corresponding current recorded each time the meniscus lands. Reproduced from ref. 95 with permission from Elsevier © 2020.

nanofabrication,[103] *etc.* AFM has been beneficial in electrocatalysis as well, for example in measuring the *operando* electrochemical potential of electrocatalysts thanks to the use of a conducting tip.[100] When AFM features are combined with the ones of SECM (AFM-SECM), their features merge and allow topographical and electrochemical measurements with high resolution and with precise control of the probe tip position. AFM-SECM image resolution is competitive to that of SICM-SECM, although the probe of the former combination is costly and has a limited reliability and durability.[83]

It's worth mentioning other SPM techniques with similar principles to AFM, such as Kelvin probe force microscopy (KPFM) and electrostatic force microscopy (EFM), which unlike AFM, are based on long range interactions and operate always in non-contact mode.[104] These methods give access to work function (WF) and local charge phenomena,[105] nowadays even with a nanometric resolution.[106] Moreover, electrochemical and ionic phenomena can be determined by electrochemical strain microscopy (ESM), a technique whose working principle consists in detecting changes in electrochemical strains of the sample.[107]

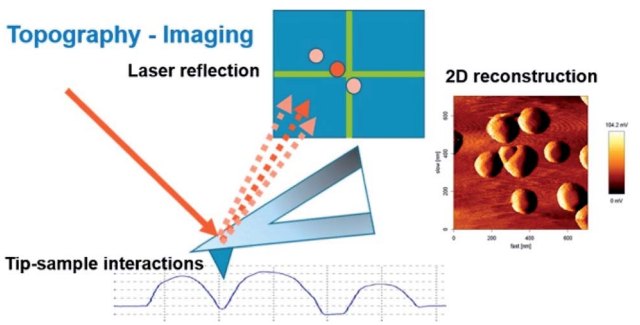

Fig. 8 Scheme of the imaging mode in AFM. Reproduced from ref. 108 with permission from MDPI © 2017.

Electrochemical reactions

The more extensively investigated electrocatalytic reactions are the ORR, OER and HER, which will be discussed in more detail herein. Noble electrocatalytic materials have been studied for these reactions, often as models to illustrate the potentiality of the technique. Even though such studies will be mentioned, this review focuses on discussing the findings on non-precious electrocatalysts. Although more limited, interesting SECM research has been reported on the CO_2RR and HOR as well and they will be presented briefly at the end of this review.

Oxygen reduction reaction (ORR)

The selective and efficient reduction of oxygen has crucial importance for the proper functionality of fuel cells. O_2 can be reduced either directly to water through a 4-electron transfer, or indirectly through a 2-electron transfer forming hydrogen peroxide as an intermediate. The reactions of both pathways in acidic and alkaline media are presented below as (2)–(7).[109] The detailed mechanism of the ORR is rather convoluted and it

Open Access Article. Published on 19 November 2020. Downloaded on 4/20/2026 1:55:05 AM.
This article is licensed under a Creative Commons Attribution-NonCommercial 3.0 Unported Licence.

depends on the electrocatalyst; however some proposed mechanisms are summarized by Nie *et al.*[110]

Acidic media

$$\text{Direct pathway: } O_2 + 4H^+ + 4e^- \rightarrow 2H_2O \quad (2)$$

$$\text{Indirect pathway: } O_2 + 2H^+ + 2e^- \rightarrow H_2O_2 \quad (3)$$

$$H_2O_2 + 2H^+ + 2e^- \rightarrow 2H_2O \quad (4)$$

Alkaline media

$$\text{Direct pathway: } O_2 + 2H_2O + 4e^- \rightarrow 4OH^- \quad (5)$$

$$\text{Indirect pathway: } O_2 + H_2O + 2e^- \rightarrow HO_2^- + OH^- \quad (6)$$

$$HO_2^- + H_2O + 2e^- \rightarrow 3OH^- \quad (7)$$

With a thin layer of the catalyst, the calculation of the number of transferred electrons per O_2 molecule namely n, through the RDE method, is typically made by using the Koutecky–Levich (K–L) equation (eqn (8)), where j = current density, j_L = current density limited by diffusion, j_K = kinetic current density, and ω = angular velocity and B is expressed as eqn (9), where F (Faraday constant) = 96 485 C mol^{-1}, C_{O_2} = bulk concentration of oxygen, D_{O_2} = diffusion coefficient and ν = kinematic viscosity of the electrolyte.[111]

$$\frac{1}{j} = \frac{1}{j_L} + \frac{1}{j_K} = \frac{1}{B\omega^{1/2}} + \frac{1}{j_K} \quad (8)$$

$$B = 0.2nF(D_{O_2})^{2/3}\nu^{-1/6}C_{O_2} \quad (9)$$

The indirect pathway would be troublesome for our purpose since the production of H_2O_2 lowers the overall efficiency. Moreover, it may degrade the membrane of the fuel cell[112] or decompose the frequently used Nafion.[113] Nevertheless, the quantification of the intermediate produced during the ORR aids in the determination of electrocatalyst selectivity. This can be done with the RRDE method, by evaluating the percentage of hydrogen peroxide through eqn (10) in which i_d is the current of the disk electrode, i_r the current of the Pt ring and N the collection efficiency of the ring.[114] This information can be used for evaluating the n as well (eqn (11)), which can be a convenient way to test the reliability of the results, by analyzing the consistency with the n evaluated by using the K–L equation.

$$\%\ H_2O_2 = 200 \times \frac{i_r/N}{i_d + i_r/N} \quad (10)$$

$$n = 4 \times \frac{i_d}{i_d + i_r/N} \quad (11)$$

SECM has been very utile for studying the ORR. The tip generation/sample collection (TG/SC) mode is often used for ORR investigation, where the tip generates O_2 and the sample collects it, thus measuring the sample current.[115] This however leads to a high background current especially on large samples which compromises the sensitivity and resolution, leading to the development of Redox Competition (RC) mode.[68] On the other hand, sample generation/tip collection (SG/TC) mode can be used for detecting H_2O_2 at the tip, while it is produced in the sample during the ORR.[116] A simultaneous combination of these three modes was introduced by Eckhard and Schuhmann,[117] enabling the determination of the activity and selectivity of electrocatalysts.

One of the main factors that predict the suitability of an electrocatalyst towards the ORR is the binding energy of O_2 with the catalyst, which is often illustrated by volcano plots.[118] The bond has to be strong enough for the oxygen to bind to the catalyst, but not too strong so it prohibits the removal of the intermediates.[118] This kind of in-between bond strength is what puts noble metal electrocatalysts on top of the volcano curve, which makes them very suitable candidates for the ORR.[119–125] However, these state-of-the art electrocatalysts are more costly; thus researchers have been developing various combinations to decrease the noble-metal loading, thus presumably decreasing the cost. For instance, Sun *et al.*[126] have prepared alloys such as PdW nanoparticles supported on nitrogen and sulfur doped graphene (NSG) and demonstrated through RC-SECM a high electrocatalytic activity for the ORR. On the other hand, Pham Truong *et al.*[127] have hosted the Pt catalyst onto a polymer brush ionic liquid (poly(IL)), which showed a promising electroactivity towards the ORR. Moreover, Kim *et al.*[128] have explored nanowires of silver chloride and bromide (AgClNWs and AgBrNWs respectively) for their oxygen reduction activity in alkaline media, using SG/TC mode and an Au UME (12.7 μm in diameter) at a d of only 5 μm. The substrate used was GC loaded with the samples and compared with a bare Pt substrate. The results for AgClNWs presented an even better activity (higher current) than Pt.[128]

In recent years, priority has been more and more given to the investigation of non-noble electrocatalysts. For instance, the ORR electrocatalytic activity of cobalt sulfide (CoS_2) relative to its morphological evolution was for the first time studied by Singh *et al.*[129] A strong dependence between specifically exposed surfaces and ORR activity was previously found for several metal oxides, possibly because of differences in surface energies.[130,131] In this work, octahedral CoS_2 crystals with {111} and {220} planes were synthesized. SECM was employed for the visualization of local electrocatalytic activity using RC mode, a GC plate as the substrate, a Pt UME in 0.1 M perchloric acid ($HClO_4$) and a tip-to-substrate distance of 10 μm. SECM results revealed a homogeneous distribution of ORR active sites throughout the catalyst. RDE and RRDE results on the other hand showed a higher ORR activity of {111} facets.

The same group analyzed manganese tungstate ($MnWO_4$) with a bird-feather (BF) like morphology, acquired by optimizing the concentration of a structure directing agent (SDA), in this case hydrated trisodium citrate (TSC). The catalyst spots synthesized with different TSC concentrations were mapped through RC-SECM mode, in which case a good agreement with RDE results was found (Fig. 9). The latter figure shows the high alteration of ORR activity with changes in substrate potential, suggesting no significant contributions from topography. One

© 2021 The Author(s). Published by the Royal Society of Chemistry

Open Access Article. Published on 19 November 2020. Downloaded on 4/20/2026 1:55:05 AM.
This article is licensed under a Creative Commons Attribution-NonCommercial 3.0 Unported Licence.

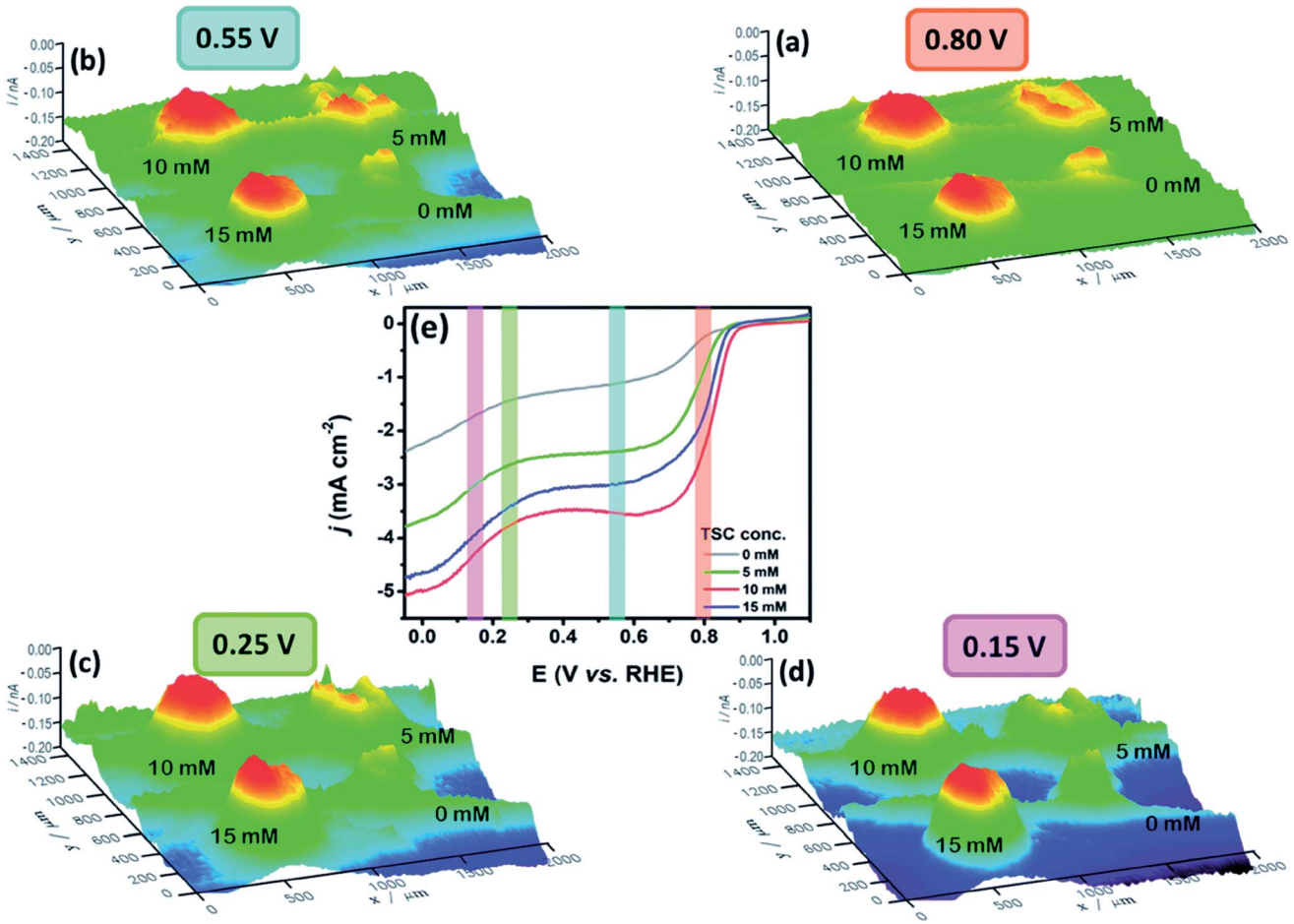

Fig. 9 ORR 3D RC-SECM images of $MnWO_4$–BF synthesized at four TSC concentrations, namely 0, 5, 10 and 15 mM at different substrate potentials: (a) 0.80 V, (b) 0.55 V, (c) 0.25 V and (d) 0.15 V. The tip (Pt UME 10 μm in diameter) was held at 0.55 V at a 10 μm distance from the sample in a 0.1 M NaOH electrolyte, (e) RDE results for the studied TSC concentrations. Counter electrode: Pt coil and reference electrode: Ag/AgCl/3 M KCl (potentials converted to the RHE scale). Reproduced from ref. 132 with permission from the Royal Society of Chemistry © 2018.

can also recognize a superior activity for 10 mM TSC concentration, along with the homogeneous distribution of active sites (red area) at all applied substrate potentials. This catalyst exhibited good electrocatalytic activity towards the ORR in alkaline media ($2 + 2e^-$ pathway), a result acquired through SG/TC mode of SECM and RRDE methods as well.[132]

The ORR investigation of nickel and cobalt-based oxides, namely NiO, Co_3O_4 and their combination (NCO) with a structure of $Ni_xCo_{3-x}O_4$, was done by Sidhureddy *et al.*[133] The measurements were conducted in alkaline media, by measuring the intermediate (HO_2^-) current through SECM in SG/TC mode, using a Pt UME of 10 μm in diameter, a GCE substrate and $d =$ 2.0 μm. The images of current produced by HO_2^- production are shown in Fig. 10, where one can see that the combination of oxides (NCO-1) exhibits the lowest HO_2^- current and hence the highest electroactivity towards the ORR, which matches also

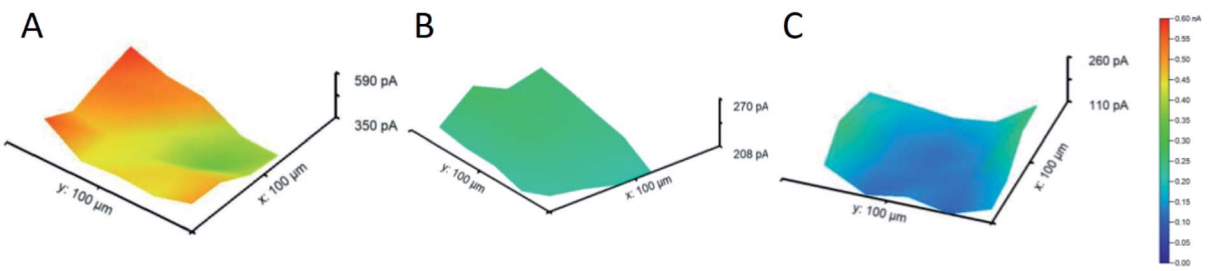

Fig. 10 SECM tip current profile for the intermediate generated at (A) NiO, (B) Co_3O_4 and (C) NCO-1. Reproduced from ref. 133 with permission from the American Chemical Society © 2019.

Open Access Article. Published on 19 November 2020. Downloaded on 4/20/2026 1:55:05 AM.
This article is licensed under a Creative Commons Attribution-NonCommercial 3.0 Unported Licence.

their results obtained by the RDE method. This may be the outcome of a higher electrical conductivity of the NCO-1 in comparison to non-mixed oxides.[134,135]

Besides metal sulfides and oxides, bare metal structures have been studied as well for their ORR activity. For instance, Michalak *et al.*[136] have examined copper nanostructures (CuNSs) by utilizing SECM in feedback mode with an Au UME of 100 μm in diameter and $d = 30$ μm. After the oxygen is generated at the Au UME, it diffuses to the sample, where it reduces again and forms OH^-, which generates a positive feedback at the UME. The effect of sample topography can be neglected considering the 30 μm distance of the sample from the flat support. The ORR activity was assessed in different electrolytes and it was found that it is elevated in electrolytes with a higher concentration of chloride ions (Fig. 11). The presence of such ions seems to fasten the formation of crystalline CuNSs rather than amorphous and less active structures. Nevertheless, selectivity was not acquired, since the intermediate could not be oxidized (detected) at the Au tip,[136] although this has been achieved by the previously mentioned work of Kim *et al.*[128]

Additionally, copper was studied for its ORR activity by Zhang *et al.*[137] with the purpose of evaluating its corrosion properties. The investigation was carried out with SECM in TG/SC mode with which the amount of H_2O_2 was determined as well. The substrate used was Pt (62.5 μm in radius) with a determined collection efficiency for H_2O_2 of 83%. A Cu tip 12.5 μm in radius was utilized at $d = 5$ μm in 0.1 M sodium perchlorate ($NaClO_4$) solution with two different pHs. The low amount of intermediate produced (20% in neutral and 10% in alkaline solution) suggested that the electron transfer occurred mostly through a four-electron transfer at both pHs.[137]

Some groups have studied electrocatalysts that are metal-free, such as Tiwari *et al.*[138] who have evaluated the performance of nitrogen-bearing carbon spheres (NCSs) synthesized at 600, 800 and 900 °C (NCS-600, NCS-800 and NCS-900). The application of metal free carbon-based nanomaterials in electrocatalysis has emerged recently, thanks to their good conductivity, high surface area and stability.[139] Exclusively the nitrogen-doped ones have the attention since the electron density of the sp^2 carbon structure is rearranged, thus activating the reduction of O_2.[140] In this work, they determined the H_2O_2 produced during the ORR by the catalyst on a GC plate (working electrode 1, WE1), using a Pt tip 10 μm in diameter (working electrode 2, WE2) above the sample at $d = 10$ μm, through SG/TC mode of SECM in 1 M potassium hydroxide (NaOH) and a loading of 50 μg cm^{-2}. The H_2O_2 current appears at the same time with the O_2 reduction current and disappears when the reduction is complete. The four-electron pathway ORR was assumed considering that the oxidative current stays constant after it decreases to the baseline. The imaging of local activity was done in the RC mode which revealed a uniform distribution of the active sites throughout the NCS-800 catalyst as the best performing catalyst according to RRDE results. The better activity of NCS-800 ($n = 3.8$, K–L plots) was attributed to the higher percentage of C–C sp^2 carbon in the structure (70%) compared to the other studied materials, which was determined by X-ray photoelectron spectroscopy (XPS) analysis.

A combination of carbon materials and metal-based compounds was made by Xin *et al.*,[141] who have investigated nanostructured hybrids based on $MoSe_2$ and reduced graphene oxide (rGO) nanosheets ($MoSe_2$@rGO) in 0.1 M KOH. $MoSe_2$ is a type of transition metal dichalcogenide (TMD) whose layered nanostructure exhibits a high surface area; however in its two-dimensional (2D) nanosheet form it has a tendency for agglomeration which compromises its capability for ORR activity.[142,143] To surpass this drawback and the fact that $MoSe_2$ has a low conductivity,[144] they combined three-dimensional (3D) $MoSe_2$ structures with highly conductive graphene-based materials. SECM measurements in RC mode with a Pt tip of 25 μm in diameter, glassy carbon electrode (GCE), $d = 50$ μm and sample loading of 510 μg cm^{-2} were performed by line scans in the *XY* plane and showed that the hybrid had the highest ORR activity compared to $MoSe_2$, rGO and their physical mixture ($MoSe_2$ + rGO), similar to the result acquired from the K–L plots (RDE method).

Similarly, Dobrzeniecka *et al.*[112] have investigated ORR dependence on the loading (70–700 μg cm^{-2}) of multiwalled carbon nanotubes (MWCNTs) and their composite with cobalt(IX) protoporphyrin (MWCNTs/CoP) in a 0.1 M phosphate buffer as the electrolyte. By utilizing a combination of redox competition and generation/collection modes of SECM,[117] the authors were able to extract the number of electrons transferred (n), amount of H_2O_2 produced, and rate constants and then compare them with the results obtained from RDE and RRDE methods. They utilized a 25 μm diameter Pt UME and $d = 30$ μm at a rigid x–y grid position. The n was quantified based on the data gathered from the reduction of oxygen and oxidation of H_2O_2 using eqn (12) which is similar to eqn (11), except that here the background current is corrected. The collection efficiency (N) was considered 100%, based on the fact that the ORR and H_2O_2 currents did not change as a function of d.[53]

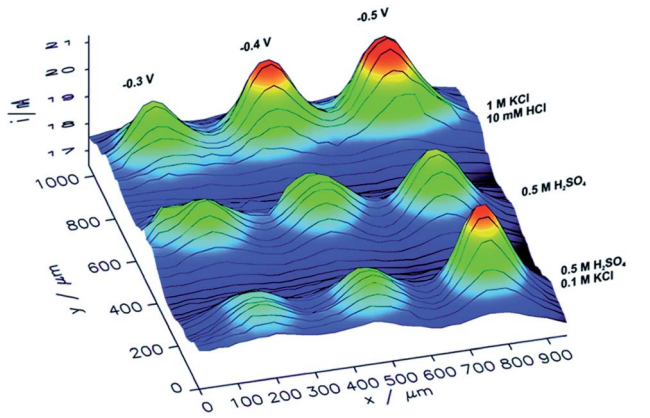

Fig. 11 ORR images of CuNS microspots deposited on indium doped tin oxide (ITO), analyzed by SECM in feedback mode, at several support potentials (−0.3, −0.4 and −0.5 V) and various electrolytes with a tip potential of +1.6 V *vs.* Ag/AgCl.[136] Reproduced from ref. 136 with permission from the Royal Society of Chemistry, © 2019.

© 2021 The Author(s). Published by the Royal Society of Chemistry

Open Access Article. Published on 19 November 2020. Downloaded on 4/20/2026 1:55:05 AM.
This article is licensed under a Creative Commons Attribution-NonCommercial 3.0 Unported Licence.

$$n = 4 \times \frac{\Delta i_{O_2}}{\left(\frac{\Delta i_{H_2O_2}}{N}\right) + \Delta i_{O_2}} \quad (12)$$

The results acquired from RDE and RRDE methods did not reveal very similar results to RC-SECM.[112] For the same thickness layers, the RRDE method revealed a relatively larger value of n compared to the SECM results. This is interpreted by suggesting that in the RRDE method the intermediate may have decomposed or undergone other reactions before it arrived in the Pt-ring for detection.[112] On the other hand, in SECM, the tip was positioned in a perpendicular manner only 30 μm above the sample and was more likely to collect a more realistic amount of H_2O_2 produced. Therefore, the lower H_2O_2 amount detected through the RRDE method may falsely lead to a higher number of electrons compared to the SECM investigation.[112]

Likewise, the superior ORR catalytic activity of a composite based on $ZnCo_2O_4$ and carbon nanotubes ($ZnCo_2O_4$/CNTs) compared to its individual components was demonstrated by Ma *et al.*[145] by means of RC-SECM. A GCE was utilized as the substrate, Pt 25 μm as the UME, d = 40 μm and an alkaline electrolyte (0.1 M KOH). The high ORR activity of the composite was credited to the synergetic effects between Zn^{2+} and Co^{3+}, and between CNTs and $ZnCo_2O_4$.[145]

The possibility to combine SECM with other methods is one of the reasons why it is such a proficient technique. For example, a simultaneous ORR and H_2O_2 measurement was

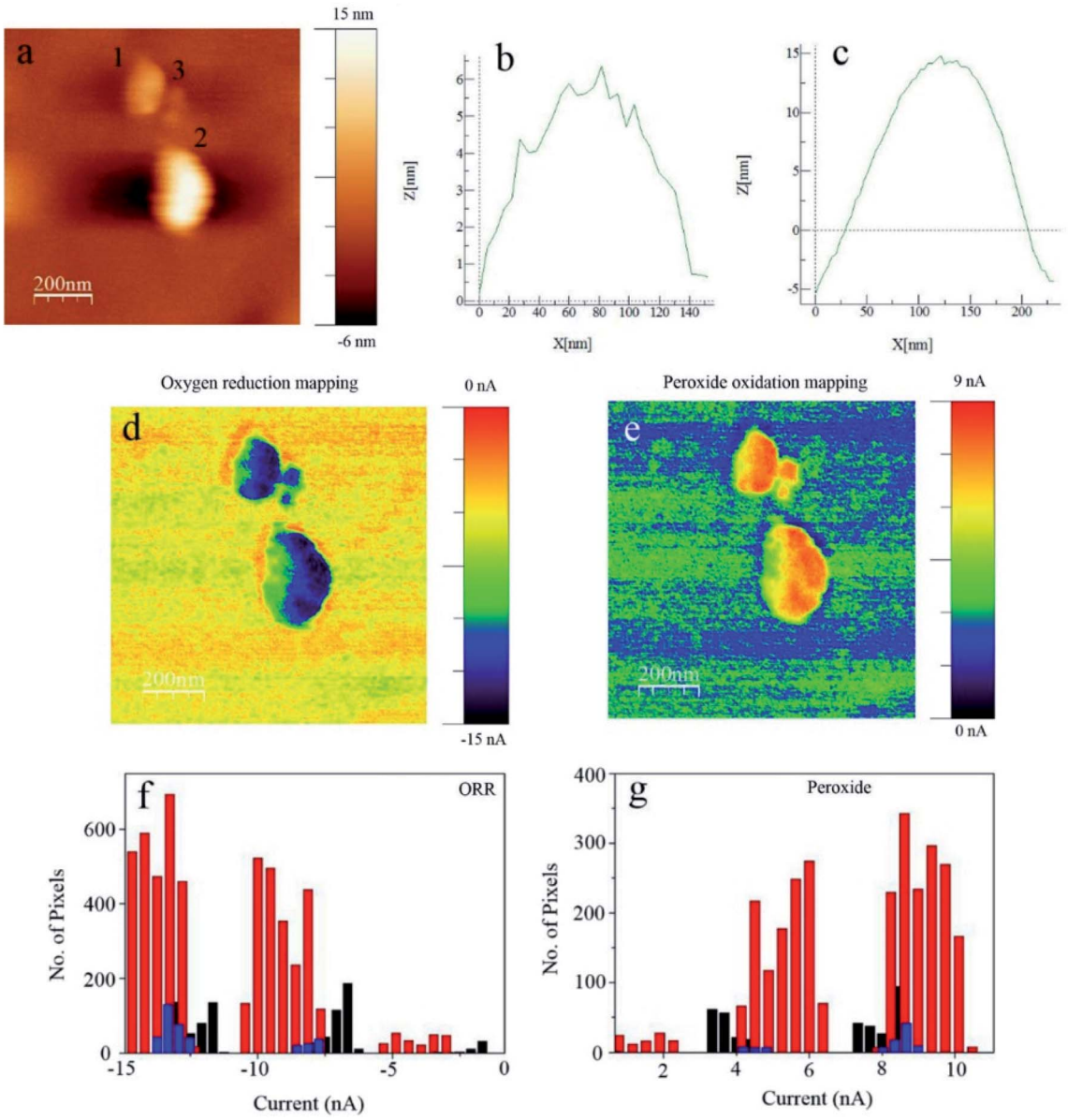

Fig. 12 Electrocatalytic current mapping through AFM-SECM on Pt NPs with an Au-c-Pt tip: (a) topography; (b and c) Z-profiles of the NPs marked '1' and '2' respectively; (d) ORR currents and (e) H_2O_2 currents of the same NPs in O_2-saturated 0.1 M $HClO_4$. $E_{substrate}$ = 0.70 V *vs.* the standard hydrogen electrode (SHE), E_{tip} = 0.98 V *vs.* SHE. Tip size, ~100 nm. Active pixel distribution of the (f) ORR and (g) H_2O_2 of Pt NPs marked as '1' in black, '2' in red and '3' in blue. Reproduced from ref. 146 with permission from John Wiley and Sons © 2019.

Open Access Article. Published on 19 November 2020. Downloaded on 4/20/2026 1:55:05 AM.
This article is licensed under a Creative Commons Attribution-NonCommercial 3.0 Unported Licence.

made by Kolagatla *et al.*[146] by joining SECM and AFM in one set-up and using SG/TC mode and an AFM-SECM dual electrode tip. The authors performed nanoscale measurements of platinum nanoparticles (Pt NPs) on a GC surface, by using an Au-coated SiO_2 Pt tip (collection efficiency ≈ 70%) at only 4–8 nm from the substrate. They determined where activity is detected and found that the pixels corresponding to ORR activity are almost the same as the ones corresponding to the H_2O_2 generated (Fig. 12). Interestingly, considering the high amount of H_2O_2 produced by the particles, the authors concluded that the Pt NPs exhibited a two-electron pathway reduction of O_2 and only half of the catalyst surface undergoes the ORR.[146] This is highly contradictive to most results obtained through the RRDE method and to the fact that Pt materials are generally accepted as the state-of-the-art ORR electrocatalyst. However, such a set-up can be beneficial for investigating electrocatalytic activity relative to the surface morphology of electrocatalysts.

Another innovative set-up was applied for ORR investigations by O'Connell *et al.*[147] through combining SECM in SG/TC mode and scanning ion conductance microscopy (SECM-SICM). The authors demonstrated the utility of the technique by mapping the ORR activity in gold nanoparticles (Au NPs) deposited on GC by utilizing a twin-barrelled pipette, in which one barrel serves as a channel of ion conductance and the other is a solid electrode which carries out the faradaic process measurements. RRDE experiments revealed the highest H_2O_2 amount (67%) at 0.4 V. This is in accordance with what was observed from the SECM-SICM images shown in (Fig. 13A), where the highest peroxide generation is at 0.4 V. It was also observed that particles with a similar size determined by SICM exhibited different peroxide detection signals (Fig. 13B and C) which may indicate possible unlike crystal structures within the ensemble.[147]

Besides the influence of heteroatom doping of carbon materials, certain defects in the structure also have been shown to modulate the electronic and catalytic properties, thus influencing the adsorption of intermediates on the catalyst.[148] Actually, even non-doped but edge-defective carbon materials have shown promising results for the ORR.[149] Nevertheless, studies on charge visualization of active sites have been lacking.

By using SICM as a charge-sensitive technique,[150] the interdependence between surface charge and electrocatalytic activity was studied by Tao *et al.*[151] in defective highly oriented pyrolytic graphite (HOPG). SICM data of pristine HOPG were acquired with a 0.5 μm nanopipette–HOPG distance. After the introduction of defects by plasma irradiation, the distance changed from 0.5 to 6.6 μm, indicating an increase in the surface charge of the sample (Fig. 14). ORR performance was better in the defective HOPG, with an onset potential of 0.745 V *vs.* the reversible hydrogen electrode (RHE) compared to 0.171 V in pristine HOPG in 0.1 M KOH.

Oxygen evolution reaction (OER)

While the oxygen evolution reaction in acidic media is presented in Fig. 1, the reaction in alkaline media is expressed by

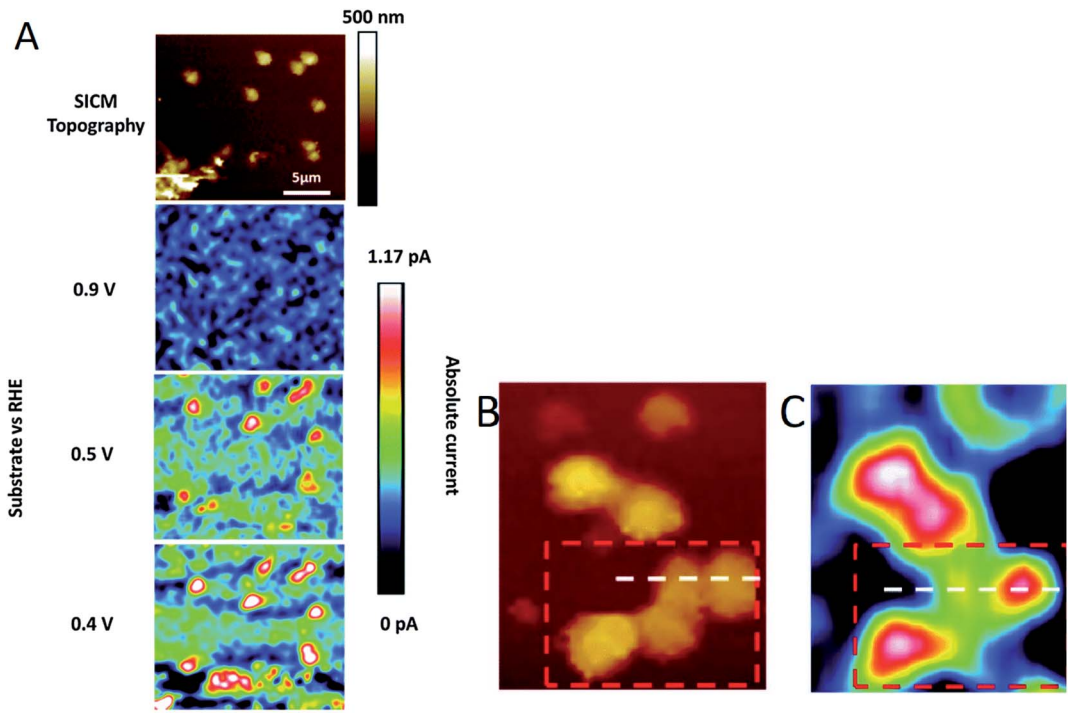

Fig. 13 SECM-SICM images of (A) Au NP ensemble electrodes at several substrate potentials (*E* converted to the RHE scale in 0.1 M NaOH) where the SECM tip is polarized at 1 V *vs.* RHE for peroxide oxidation. Magnified area of a high density ensemble with surface biased at 0.3 V *vs.* RHE is shown in (B) SICM topography and (C) the corresponding peroxide detected with SECM. Rectangle mark represents the cluster of particles discussed in the text and the white line the cross section position for highlighting particles with different peroxide signals.[147] Reproduced from ref. 147 with permission from the Royal Society of Chemistry, © 2015.

© 2021 The Author(s). Published by the Royal Society of Chemistry

Open Access Article. Published on 19 November 2020. Downloaded on 4/20/2026 1:55:05 AM.
This article is licensed under a Creative Commons Attribution-NonCommercial 3.0 Unported Licence.

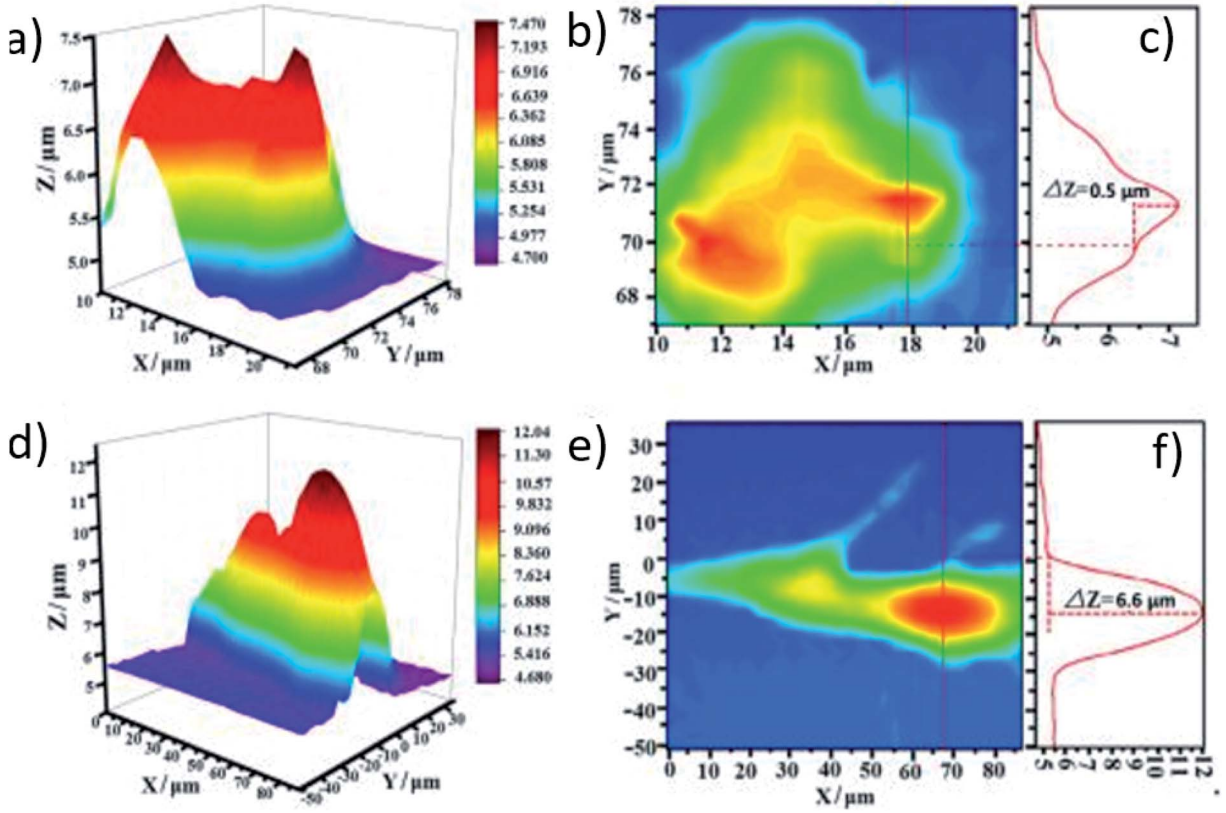

Fig. 14 (a and b) Topography 2D/3D image and (c) respective profile perpendicular to the stripe of pristine HOPG. (d and e) 2D/RD topography image and (f) extracted profile perpendicular to the stripe of defective HOPG. The before and after plasma irradiation images (pristine and defective HOPG, respectively) correspond to the same sample region. Reproduced from ref. 151 with permission from John Wiley and Sons © 2019.

eqn (13).[152] The OER occurs *via* a 4-electron transfer, preferably through single-electron transfers at each of multi-step reactions through which it takes place.[152] Several studies have been dedicated to unraveling the mechanisms of the OER in acidic and alkaline media in a variety of materials.[153–157]

$$4OH^- \rightarrow 2H_2O + O_2 + 4e^- \quad (13)$$

Lithium intercalated nickel phosphorus trisulfide ($NiPS_3$) nanosheets of less than 1 nm in thickness were investigated in alkaline media for their OER onset potential by Konkena *et al.*,[158] using SECM in SG/TC mode with a 800 nm diameter nanoelectrode and $d = 4$ μm. The onset potential has a value of 1.48 V *vs.* RHE where there is an abrupt rise in current, a value which corresponds well to the ones present in the literature at that time.[159,160] The metallic-edge sites and defects available in the catalyst structure were associated with the promising OER activity, along with the high conductivity of $NiPS_3$.[158]

An interesting and rapid approach for studying the OER in individual catalyst spots by SECM in SG/TC mode was introduced by Minguzzi *et al.*[161] In order to hamper the expansion of the diffusion layer from the O_2 produced, potential steps were applied with values that correspond to the OER activity and non-activity of the sample. Digital simulation was used in order to establish the conditions for preventing the overlap of diffusion layers that are developed at each spot.[161] Then, using this approach, the authors studied the OER activity of a mixture containing SnO_2–IrO_2. It was found that the OER activity was higher with an increase in the percentage of IrO_2 in the sample, a trend which was in agreement with the results in the literature for the same sample, thus proving the validity of the introduced approach. Besides, this way enabled the usage of a conventional SECM tip instead of the metal-shielded one[162] and a shorter time frame for the total experiment.[161]

Surface-interrogation (SI-SECM) was employed by Ahn and Bard[48] with the purpose of analyzing the active atoms in the surface of the well-known OER electrocatalyst CoP_i and the reaction rate constants, by amperometric titrations of Co^{III} and Co^{IV} with 1,1′-ferroceniumdimethanol ($FcDM^+$) or K_2IrCl_6. Two Au electrodes were used as the substrate (where the catalyst is deposited) and collector (which detects the analyte), both with a size of $a = 12.5$ μm and separated by 1.7 μm from each other. The principle consists in applying positive potential pulses on the substrate which generate Co^{III} and Co^{IV} and then scanning the tip to potentials which reduce $FcDM^+$ to FcDM, so that the last one can be oxidized again from Co^{III} and Co^{IV} generated previously at the substrate (Fig. 15). From the plateau in the acquired plots of charge density *vs.* substrate potential it was possible to extract the density of Co atoms that are available to water. The density of the active sites on the surface of the

Open Access Article. Published on 19 November 2020. Downloaded on 4/20/2026 1:55:05 AM.
This article is licensed under a Creative Commons Attribution-NonCommercial 3.0 Unported Licence.

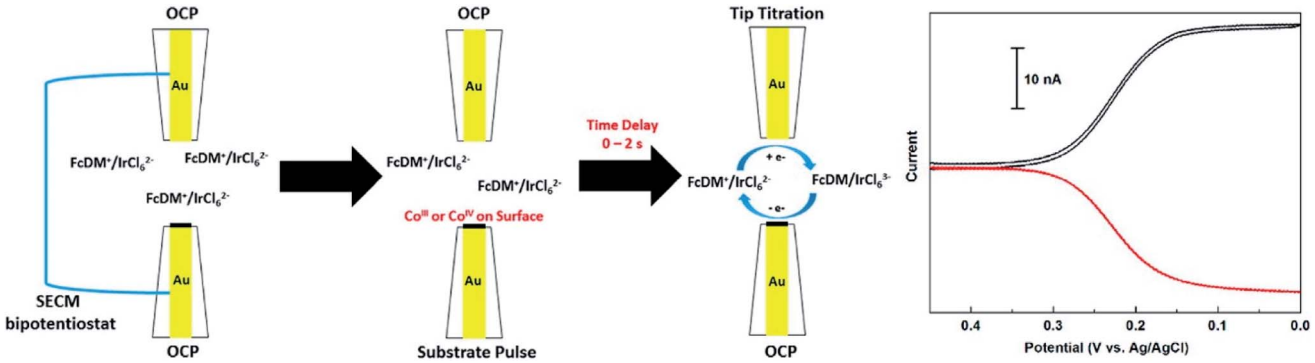

Fig. 15 Scheme of the SI-SECM setup and the feedback response (on the right) representing the substrate detection of the analyte generated at the tip ($FcDM^+$ reduction at the tip). The tip current is expressed in black and substrate current in red. The concentrations of FcDM and $IrCl_6^{2-}$ were 1.2 and 1.1 mM respectively. Reproduced from ref. 48 with permission from the American Chemical Society © 2015.

catalyst was found to be 11 Co per nm^2 (comparable to the literature[163]), while the pseudo-first-order rate constants of both cobalt species with H_2O were 0.19 s^{-1} for Co^{III} and >2 s^{-1} for Co^{IV}.

On the other hand, Kim *et al.*[164] have used gold UMEs (a = 12.5 μm) separated by 3.8 μm from each other, to analyze the OER active iron atoms on hematite (α-Fe_2O_3) grown on F-doped tin oxide coated glass (FTO). The reaction was light-driven, so the catalyst thin film has a pinhole underneath the substrate in order to let the light in, while ferrocenemethanol ($FcMeOH^{+/0}$) was used as the mediator. Initially, Fe^{3+} is present in the substrate, until it is subjected to light, after which Fe^{4+} is generated which is responsible for the evolution of O_2. Afterwards, $FcMeOH^+$ gets reduced to $FcMeOH^0$ which then reduces Fe^{4+}. As a result, the density of photo-active atoms was evaluated to be 18 Fe per nm^2 at several substrate potentials and the pseudo-first order reaction rate constants evaluated by time-dependent titration were 0.03 to 0.19 s^{-1}. In another study, active site densities of layered double hydroxides (LDHs) and amorphous Ni–Fe (oxy)hydroxides ($Ni_{1-x}Fe_xOOH$) were determined *in situ* through SECM by Barforoush *et al.*[165] The authors found that the density of active sites is much higher in $Ni_{0.8}Fe_{0.2}OOH$ LDH (4500 sites per nm^2) than the rock salt $Ni_{0.8}Fe_{0.2}$ oxide (500 sites per nm^2), owing to the presence of Ni^{IV}/Fe^{IV} formed by water and hydroxide below the electrode/electrolyte interface.

An issue related to the study of the OER is the appearance of surface oxides in metal electrodes before the onset of the OER; thus studying alteration in the composition and surface structure of the catalysts is important in this field.[166] Arroyo-Currás and Bard[166] studied the surface species ($-OH_{(ads)}$ and $-H_{(ads)}$) formed at the surface of the catalyst (polycrystalline Ir UMEs) by using Fe(III/II)–TEA as a mediator at a very basic pH (2 M NaOH) through SI-SECM. The size of the used Ir substrate UME was a = 62.5 μm and the GC tip electrode a = 50 μm. In Fig. 16 in red, the first Ir oxide can be seen around −0.88 V and the oxide growth continues between −0.85 and −0.47 V, where OH– gets adsorbed on the substrate, in which case the coverage of the substrate is $\theta < 1$. On the other hand, the first $H_{(ads)}$ can be seen in green around −0.70 V, followed by an increase in surface

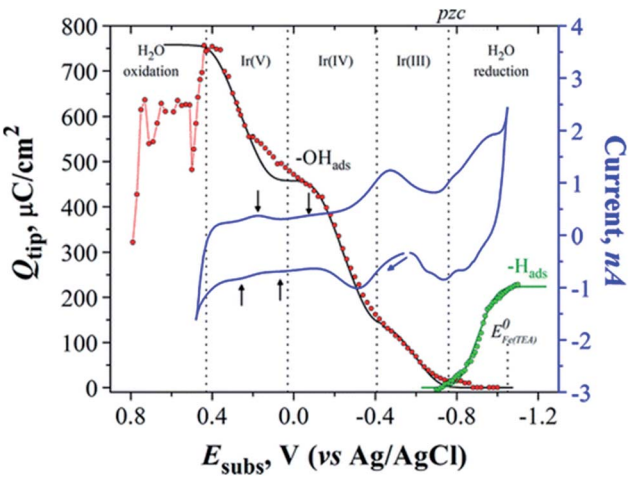

Fig. 16 Q_{tip} *vs.* E_{subs} plots acquired by the interrogation of transients of the two adsorbed species on Ir ($-OH_{(ads)}$ and $-H_{(ads)}$), the former being interrogated with 10 mM Fe(II)–TEA (red dots) and the latter with 1 mM $FcMeOH^+$(green dots). ΔE_{sub} = 0.01 V and each dot represents an individual SI-SECM measurement. Blue line: CV of Ir UME in 2 M NaOH; v = 20 mV s^{-1}. Black and green lines: Frumkin isotherm fits, using g' = −6 and g' = −2 respectively. Red line: order in which the data were obtained at ΔE_{subs} > 0.44 V. Reproduced from ref. 166 with permission from the American Chemical Society © 2015.

coverage forming a monolayer of hydrogen atoms (−0.70 to −1.10 V). In a certain potential region (~120 mV), these two species coexist in the substrate surface, marked as *pzc* in Fig. 16, where the green and red plots overlap, assuming that these species are not quite free to move in the surface. In blue we can see the cyclic voltammogram (CV) of Ir, where one can recognize several small waves indicated by black arrows, which correspond well to a charge density increase, ascribed to transformation processes in the surface such as: dehydration of $-OH_{(ads)}$ to $-O_{(ads)}$ or oxide growth. This was assumed since in a potential range between −0.03 and 0.2 V the titration curve (red) is constant, excluding the possibility of any faradaic process occurring in that range. The charge density of one monolayer of the adsorbed species was quantitatively

© 2021 The Author(s). Published by the Royal Society of Chemistry

Open Access Article. Published on 19 November 2020. Downloaded on 4/20/2026 1:55:05 AM.
This article is licensed under a Creative Commons Attribution-NonCommercial 3.0 Unported Licence.

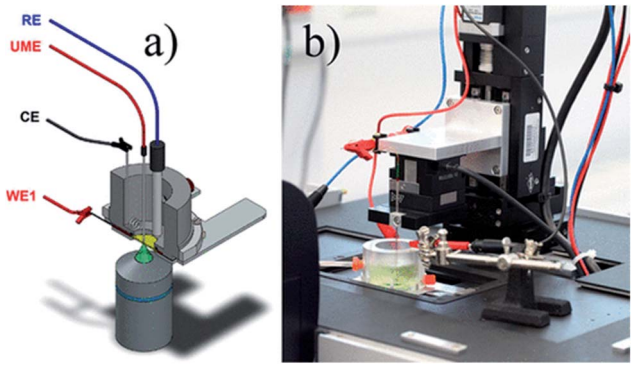

Fig. 17 (a) Setup developed for the *in situ* measurements, the used electrodes (here WE1 is a thin film electrode) and the Raman microscope from below; (b) picture of the installed instrument. Reproduced from ref. 167 with permission from the American Chemical Society © 2017.

determined and the following results were found: $Q_{\theta=1,OH} = 456 \pm 2.0$ μC cm^{-2} and $Q_{\theta=1,H} = 224.2 \pm 0.2$ μC cm^{-2} for –OH$_{(ads)}$ and –H$_{(ads)}$ respectively.

Another innovative way to take advantage of SECM is by combining it with Raman spectroscopy and perform spectroelectrochemical measurements, where a single Raman measurement is executed during all the applied potentials. Steimecke *et al.*[167] have made an investigation of the OER electroactivity of nickel/iron (Ni/Fe) and Ni thin films by using such a combined set-up, which besides probing the local electrochemistry, also allows the extraction of information on the structure or oxidation state changes in the materials during the electrochemical reaction. The measurement is done in such a way that the SECM UME is placed in proximity above the substrate and the Raman probe is placed beneath the substrate (Fig. 17). SG/TC mode is used as one would expect, by using a 25 μm Pt UME deposited in ITO and in a 0.1 M KOH electrolyte.

The recorded substrate potential, besides the OER, also corresponds to the oxidation of Ni(OH)$_2$ to NiOOH and the generation of the latter was determined by the Raman double band at 475 and 557 cm^{-1}. Besides NiOOH, Fe impurities also play a role in the OER performance of nickel oxide and hydroxide films.[168,169] In Fig. 18 one can see the dependence of Fe impurity quantity on the I_{475}/I_{557} ratio and onset potential, where the increase of Fe presence results in an increase of γ-NiOOH disorder. While up to 15% Fe percentage leads to a decrease in onset potential, higher percentages seem to have a contrary effect.

Bifunctional electrocatalysts for the ORR and OER

Separately, OER or ORR electrocatalysts find utility in many applications[152,170–173] and several reviews have covered a diversity of materials that have been studied for their ORR[174–178] and OER activity[179–183] with hydrodynamic methods. However, for regenerative fuel cells a bifunctional electrocatalyst for both reactions is required.[184] This is considered as a challenge, knowing that the ideal ORR electrocatalyst is not on top of the OER volcano as well, and *vice versa*.[185]

Nevertheless, many advancements have been made in this direction by utilizing SECM. For instance, Seiffarth *et al.*[186] have synthesized a catalyst by combining an oxide $Ni_{0.9}Co_{0.1}Fe_2O_4$ with nitrogen doped carbon nanotubes (NCNTs) and investigated its electrocatalytic activity by utilizing a loading of only 20 μg cm^{-2}. The applied pulse profile introduced in 2007 (ref. 117) was used to assess ORR activity, in an indium doped tin oxide (ITO) substrate and an UME of Pt 25 μm in diameter at $d = 25$ μm. The number of electrons was calculated by using eqn (12), and the collection efficiency was assumed to be 100%, considering that the variation of the tip-to-sample distance in a range of 10–15–35 μm did not significantly affect the ORR and H_2O_2 currents.[53] The current densities of ORR and H_2O_2 oxidation are presented in Fig. 19A and B, along with the corresponding n values of the mixed oxide, the NCNTs, their combination and the heated combination. They all show roughly a four-electron transfer, while the slight decrease in the activity of the heated combination was associated with the reduction of FeNiCo oxides.[186]

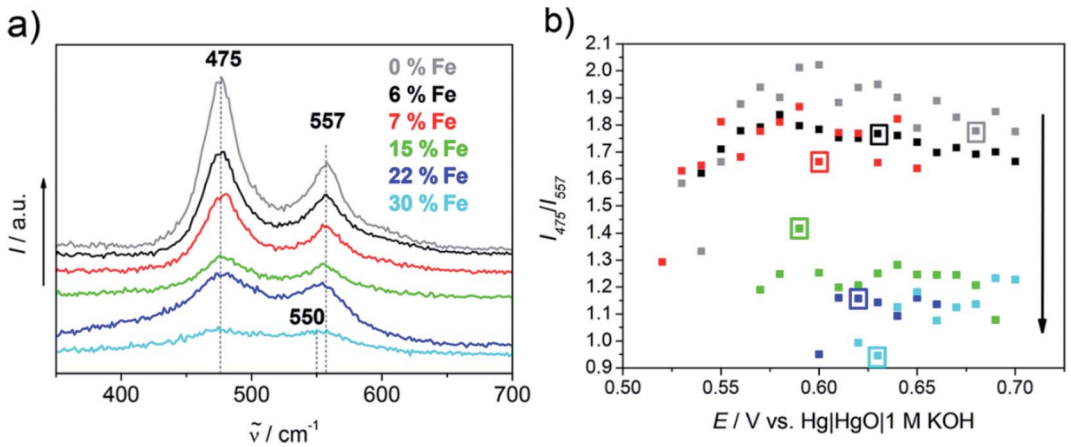

Fig. 18 (a) Raman spectra of all Ni and Ni/Fe samples at 0.63 V; (b) ratio of band intensity *vs.* applied potential. The SECM determined onset potential is marked for each sample by a square frame in the respective color, while the black arrow represents the increase of the Fe content with a lower I_{475}/I_{557} band ratio. Reproduced from ref. 167 with permission from the American Chemical Society © 2017.

Open Access Article. Published on 19 November 2020. Downloaded on 4/20/2026 1:55:05 AM.
This article is licensed under a Creative Commons Attribution-NonCommercial 3.0 Unported Licence.

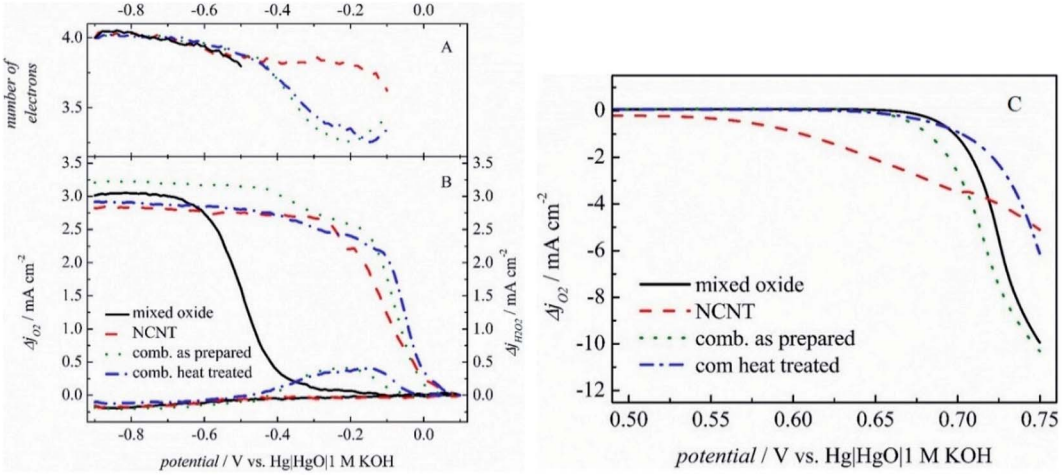

Fig. 19 (A) Number of transferred electrons and (B) current densities acquired in RC-SECM mode for ORR and H_2O_2 oxidation, with a corrected baseline. (C) Tip currents while the tip was held at −0.60 V and a linear potential sweep was applied at the substrate. Reproduced from ref. 186 with permission from John Wiley and Sons © 2016.

The OER was analyzed by SECM in SG/TC mode, by applying a constant potential at the UME which reduced the oxygen produced by the electrocatalyst. The NCNT onset potential (estimated at −0.1 mA cm^{-2}) is the most promising; however the current densities achieved by the mixed oxide and the combined electrocatalyst are the highest (Fig. 19C). As a conclusion, the combined catalyst exhibited the best results among its peers for both reactions. The voltage gap acquired from RDE experiments and SECM was 0.868 V and 0.773 V respectively. This difference in values exists supposedly because the measurement of current in SECM takes place at the UME, while in linear sweep voltammetry (LSV) measurement it takes place at the catalyst layer.[186]

By adopting a similar methodology to SECM, and hence sequential pulses for obtaining H_2O_2 and ORR currents and SG/TC mode for OER current, Chen *et al.*[56] have studied nickel and cobalt-based oxides (Ni_xO_y and Co_xO_y respectively) embedded in nitrogen doped carbon (NC) for their bifunctional electroactivity. Normalized SECM images were obtained to illustrate oxygen reduction, oxygen evolution and hydrogen peroxide production. The ORR results suggest the best activity for Co_xO_y/NC considering that it has the lowest H_2O_2 and highest ORR current. It was concluded that the carbon supported oxides show generally good activity for both reactions, while NiO is more active for the OER than the ORR.

On the other hand, Chakrabarty *et al.*[187] have demonstrated the bifunctional electroactivity of flower-like $ZnCo_2O_4$ grafted onto a reduced graphene oxide (rGO) sheet by studying both reactions with SECM in SG/TC mode at a mass loading of 150 μg cm^{-2}, using an ITO substrate, a Pt 25 μm UME and 1 M KOH. The potential gap of rGO–$ZnCo_2O_4$ between the ORR and OER was 0.679 V, which was considered by the authors as a satisfactory value compared to the ones present in the literature. Besides the high conductivity provided by the rGO layer, the promising bifunctional activity was ascribed also to the mixed oxidation state of Co (2^+ and 3^+) ions in $ZnCo_2O_4$, along with the porous nature of the metal oxide which provides a high catalytic surface area.[187]

Similarly, three-dimensional nanosheet-structured composite materials based on carbon supports and metal oxides ($NiCoO_2$/CNTs) were studied by Ma *et al.*[188] by comparing the performance to that of up-to-date electrocatalysts. The RDE and RRDE results were supported by SECM measurements in RC-SECM mode for oxygen reduction and SG/TC mode for oxygen evolution. They used a GCE as the substrate, Pt 25 μm in diameter, 0.1 M KOH, $d = 50$ μm and sample loading of 510 μg cm^{-2}. The SECM images confirm the results of RDE and RRDE methods, by proving a superior local activity of the composite compared to distinct $NiCoO_2$ and CNTs, and a similar activity to the state-of-the-art electrocatalysts.[188] The prevention of composite aggregation and the supply of extensive active sites by the carbon support may be the reason behind the good activity of $NiCoO_2$/CNTs, along with the synergetic effect between Ni^{2+} and Co^{2+}.[188]

Recently, the ORR/OER activity of cobalt-based metalloids (Co_xB and Co_xP) introduced into a nitrogen-doped carbon matrix (NC) was analyzed by Barwe *et al.*[189] A GCE substrate was used, along with a Pt UME of 25 μm diameter at $d = 12.5$ μm and sample loading 500 μg cm^{-2}. SG/TC mode was employed for H_2O_2 evaluation. It is worth mentioning that in some earlier studies,[53,112] the collection efficiency was determined by evaluating the change in currents in a certain range of tip-to-substrate distances. Here, they established it by utilizing a sample electrode that reduces oxygen in a 2-electron pathway (Hg), by applying a constant potential of −0.4 V *vs.* Ag/AgCl 3 M KCl at the Hg and of 0.7 V at the UME. Then, the calculation was done using the tip and sample currents through the expression $CE = -i_{tip}/i_{sample}$ which gave a value of 3.7×10^{-4}. Afterwards, the number of electrons was calculated with the previously established eqn (12). The authors concluded that both Co_xB/NC and Co_xP/NC exhibited selective reduction of oxygen to OH^- with a nearly 4-electron transfer and low overpotentials for both

© 2021 The Author(s). Published by the Royal Society of Chemistry

Open Access Article. Published on 19 November 2020. Downloaded on 4/20/2026 1:55:05 AM.
This article is licensed under a Creative Commons Attribution-NonCommercial 3.0 Unported Licence.

reactions. The ORR/OER round-trip voltage was determined to be 0.81 V. The good performance of the catalyst was linked to the pyridinic and pyrrolic nitrogens in the structure and to boron and phosphorus moieties combined with the Co ions and/or atoms.[189]

Even though carbon nanotubes are generally acknowledged for their high conductivity, their resistance can further be decreased by more than 50% if they form hybrids with graphene, due to enhanced effectiveness of charge tunneling.[190] Lately, such a hybrid electrocatalyst based on graphene nanoflakes (GFs) and carbon nanotubes (CNTs) doped with heteroatoms such as N, Co and Mo (N–Co–Mo–GF/CNT) was studied for its ORR and OER activity by Tavakkoli *et al.*[51] The OER catalytic activity was investigated by means of SECM in SG/TC mode in alkaline media on two different substrates, namely nickel (Ni) and glassy carbon (GC). When GC was used, the tip response (increase of ORR current) was almost simultaneous with the oxygen generation (OER onset potential), compared to the Ni substrate in which case the tip response was delayed (Fig. 20), indicating a more rapid release of oxygen by GC. This was confirmed as well by simulation studies at different layer thicknesses. In this way the authors were able to reveal that the OER at the Ni substrate occurred at the catalyst/substrate interface, while on GC it occurred close to the surface of the catalyst. The RDE measurements of the OER revealed an enhanced activity of the catalyst on the Ni substrate with an onset overpotential ($\eta_{OER,10}$) of ~50 mV lower compared to the GC substrate. As for the ORR, the number of transferred electrons was evaluated by using a RDE and K–L equation and was close to 4 for the catalyst on all studied substrates. The promising bifunctional electrocatalytic activity was attributed to the synergistic effect between the N–C and M–C sites in the catalyst structure.[51] Finally, this work demonstrates how SECM can be helpful in resolving the location where the OER occurs, and also how the substrate choice plays an important role in the activity of the electrocatalyst.

Hydrogen evolution reaction (HER)

The hydrogen evolution reaction in acidic media is presented in Fig. 1 and the reaction in alkaline media is shown below:[191]

$$2H_2O + 2e^- \rightarrow 2OH^- + H_2 \quad (14)$$

In general, in acidic and alkaline media the HER can occur *via* two steps (reactions (16)–(18)).[192–195] For instance, in alkaline media, first H_2O which is adsorbed at the catalyst surface gets reduced to a hydrogen atom (Volmer step):

$$H_2O + e^- \rightarrow H_{ads} + OH^- \quad (15)$$

Then, the H_{ads} can couple with another H_{ads} to form H_2 which escapes the surface (Tafel step):

$$H_{ads} + H_{ads} \rightarrow H_2 \quad (16)$$

Or the H_{ads} reacts with a H_2O molecule to produce H_2 (Heyrovsky step):

$$H_{ads} + H_2O + e^- \rightarrow H_2 + OH^- \quad (17)$$

One of the factors that can dictate the mechanism in which hydrogen evolves is the strength of the metal–hydrogen bond.[196]

The up-to date electrocatalysts for the HER occupying the top of the volcano plot are noble metals,[196] which were recently studied by SECM, for example by Fernández and Zoski,[197] who investigated noble nanoparticles for their HER performance in acidic media. They performed electro-deposition of Pt nanoparticles on gold nanoelectrode ensembles of UME dimensions, and studied them in SG/TC mode, through which they found matching results with polycrystalline Pt. Similar results were found as well for the Au nanoelectrode ensembles compared to polycrystalline Au.[197]

Moreover, nanocomposites based on palladium/titanium oxide (Pd/TiO_2) and multi-walled carbon nanotubes (MWCNTs) were investigated by Valenti *et al.*[198] for their HER

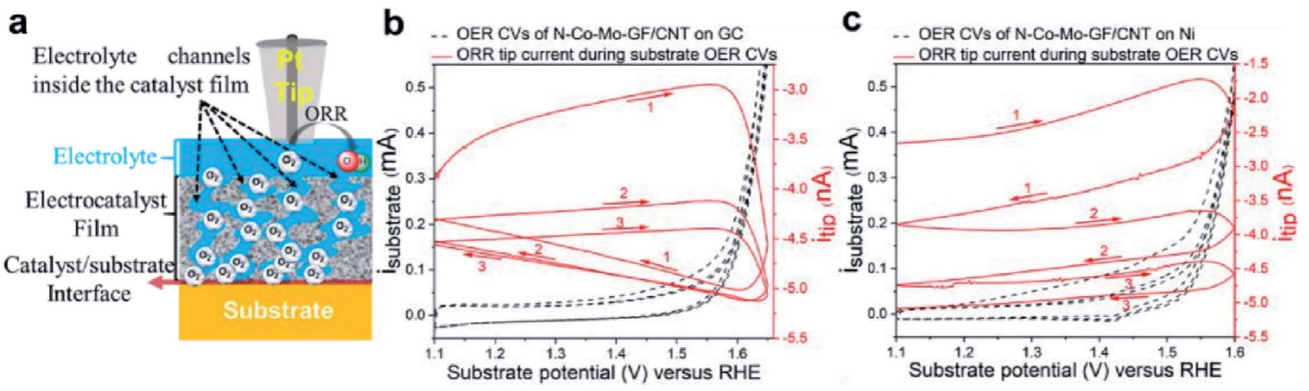

Fig. 20 (a) Scheme of the reaction where the Pt SECM tip approaches the electrocatalyst to observe the feedback from the sample and substrate, as well as the O_2 diffusion from the substrate/catalyst interface to the tip. (b and c) SG/TC results, with the tip polarized at 0.3 V *vs.* RHE for driving the ORR, while the substrate was scanned in the OER region at 5 mV s^{-1}. The tip was in proximity to N–Co–Mo–GF/CNT on (b) GC and (c) Ni substrates. Reproduced from ref. 51 with permission from American Chemical Society © 2020. https://pubs.acs.org/doi/abs/10.1021/acscatal.0c00352. Further permissions related to this material should be directed to the American Chemical Society.

© 2021 The Author(s). Published by the Royal Society of Chemistry

Open Access Article. Published on 19 November 2020. Downloaded on 4/20/2026 1:55:05 AM.
This article is licensed under a Creative Commons Attribution-NonCommercial 3.0 Unported Licence.

activity by using SG/TC mode of SECM in a neutral pH electrolyte. As anticipated, the introduction of MWCNTs increases the HER activity of Pd/TiO_2, possibly due to improved pairing of palladium electronic levels at the interface of TiO_2/MWCNTs which exhibits enhanced surface states.[198]

However, as mentioned earlier, non-noble electrocatalysts are advantageous and they have been the focus of research for HER activity in the past few years. For instance, transition metal dichalcogenides have shown promising performance towards the HER,[199–201] in which the disulfide-terminated edges play the role of catalytic sites for hydrogen evolution.[200]

Hyper thin one-dimensional (1D, wires) and two-dimensional (2D, discs) FeS_2 nanostructures were studied for their HER activity at neutral pH by Jasion *et al.*[202] in SG/TC mode of SECM, by polarizing the sample at a negative potential for hydrogen evolution and the tip at a positive hydrogen-oxidation potential. The substrate used was a GCE and a 200 μm Pt tip at d = 100 μm. The results were compared with those of a Pt substrate as the state-of-the art HER electrocatalyst and with those of a bare glassy carbon electrode (Fig. 21). The authors conclude that the HER occurred at the 2D FeS_2 sample at an overpotential of less than 50 mV higher than that at the Pt catalyst. Moreover, faradaic efficiency which represents the ratio of the experimental quantity of hydrogen evolved and the theoretical quantity[203] was determined for the discs by means of SG/TC mode, with a 200 μm Au substrate modified with the sample (FeS_2 discs) and it was found to have a value of 92 ± 8%.[202] The highlight of this work was the better HER activity of the 1D and 2D FeS_2 nanostructures compared to the 3D cube structures.

A CoS_x electrocatalyst obtained from metal–organic frameworks (MOFs) *via* an SECM tip-induced method was subsequently analyzed for its HER behavior by Liberman *et al.*[47] SG/TC mode was used with a 10 μm Pt tip at $d = 11.5 \pm 0.5$ μm in a ring-shaped ~100 μm CoS_x sample. The alike diameter of the patterned sample and the glass-coated tip leads to a high collection efficiency, needless of using an UME as a substrate. The HER mapping is presented in Fig. 22, whereas the shape of the sample pattern was confirmed as well by energy-dispersive X-ray spectroscopy (EDS). As a conclusion, the authors successfully combined localized catalyst fabrication and its

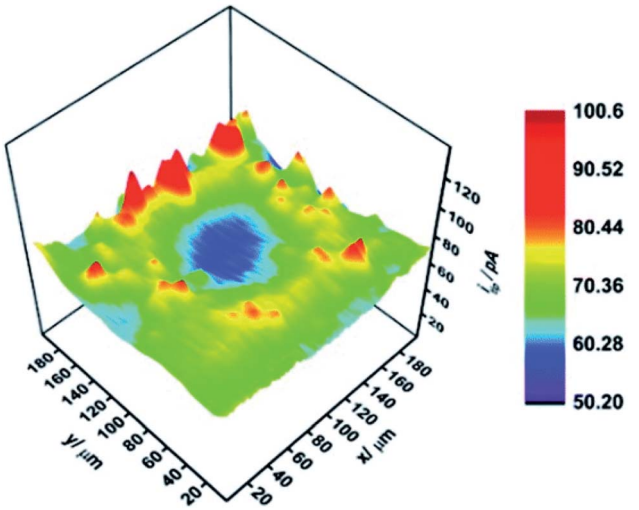

Fig. 22 Hydrogen evolution reaction activity map of the as-prepared 60× localized electrochemical conversion pattern.[47] Reproduced from ref. 47 with permission from the Royal Society of Chemistry, © 2020.

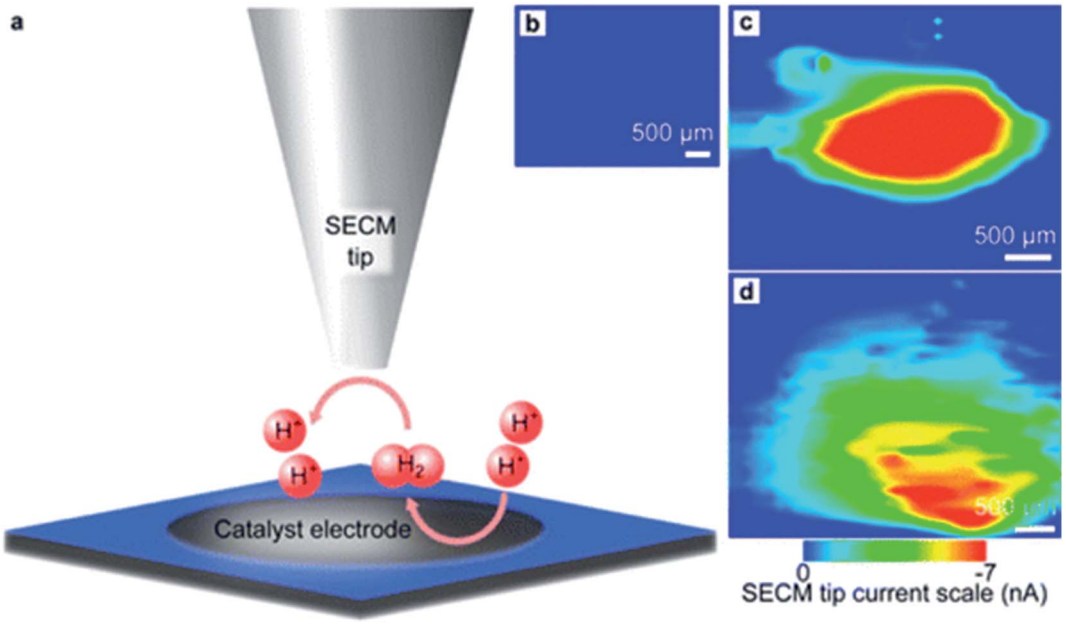

Fig. 21 HER electroactivity maps acquired *via* SECM: (a) scheme of the SECM experiment (SG/TC mode), (b) the reactivity map of a glassy carbon electrode, (c) HER electrochemical reactivity map of Pt on glassy carbon and (d) HER electrochemical reactivity map of FeS_2 discs on glassy carbon. Reproduced from ref. 202 with permission from the American Chemical Society © 2015.

© 2021 The Author(s). Published by the Royal Society of Chemistry

Open Access Article. Published on 19 November 2020. Downloaded on 4/20/2026 1:55:05 AM.
This article is licensed under a Creative Commons Attribution-NonCommercial 3.0 Unported Licence.

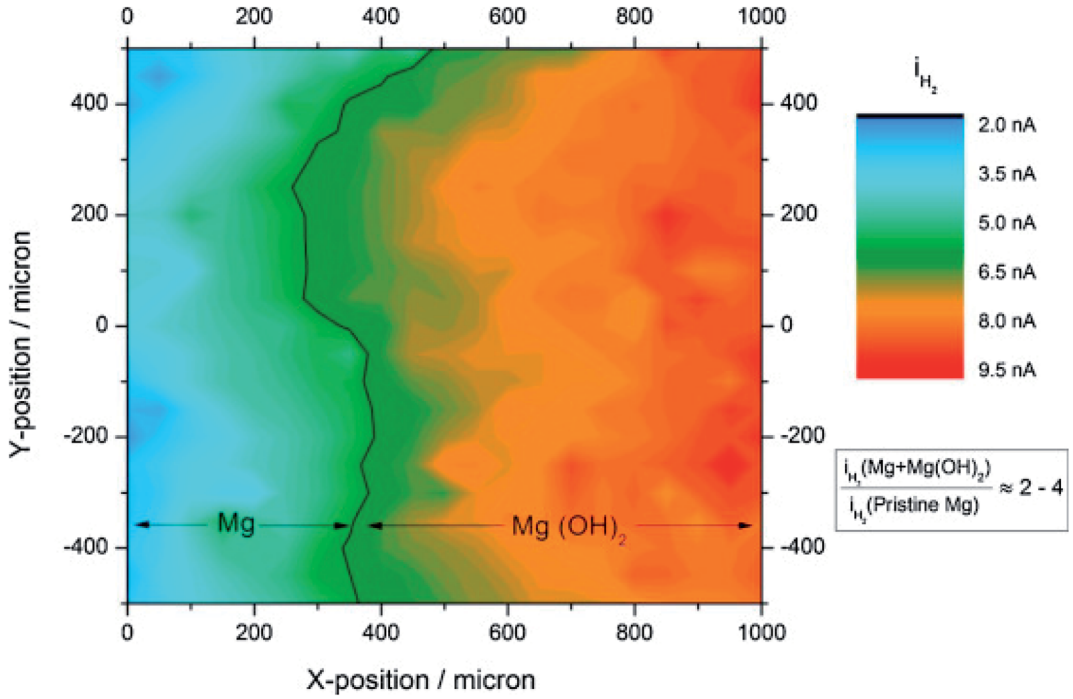

Fig. 23 SECM HER image recorded from pristine Mg across to the Mg coated with a $Mg(OH)_2$ surface. A normalization of microelectrode currents with respect to the average current of pristine Mg was done. The microelectrode was rastered with a sweep velocity of 50 μg s^{-1} and the electrochemical measurements were performed at steps of 100 μm per point. Reproduced from ref. 204 with permission from Elsevier © 2015.

consecutive SECM analysis, which is believed to be a useful approach for forthcoming screening of electrocatalysts and for the design of patterned arrays.[47]

The higher HER activity of $Mg(OH)_2$ coated on Mg, compared to pristine Mg, was demonstrated by Salleh *et al.*[204] by using SECM in SG/TC mode (Fig. 23). A 25 μm diameter Pt tip was used for the detection (oxidation) of hydrogen, at a fixed tip-to-substrate distance of 30 μm in 0.1 M NaCl solution. The hydrogen evolution rate of the $Mg(OH)_2$ coated Mg surface was determined to be ~2 to 3 times higher compared to pristine Mg, a result which was compatible with the potentiodynamic polarization measurements. These results are associated with the activation of H_2O self-dissociation in the presence of the adsorbed OH^- groups.[204] It's worth mentioning that the topographical alteration did not significantly affect the currents measured at the microelectrode, because the HOR is not a diffusion-controlled reaction on the Pt surface. The aforementioned outcome can be very important when it comes to the efficiency of systems that are based on Mg.[205,206]

A widely investigated catalyst for the hydrogen evolution reaction is molybdenum disulphide (MoS_2),[207–209] in which the edge sites play an active role in the HER,[210] while the basal planes were considered inert[211] until they were activated through creation of sulphur vacancies.[144,212] Li *et al.*[211] employed SECM in SG/TC mode in combination with multiphysics modelling in order to study the kinetics of S vacancies on monolayers of MoS_2, using the following conditions: 0.1 M $HClO_4$ electrolyte, 25 μm diameter Pt UME at $d = \sim 4$ μm and $d = \sim 5$ μm for SV-MoS_2 (unstrained area) and V-MoS_2 (strained area) respectively. The activities of strained and unstrained areas were compared and in both cases the SECM results show a fast decrease in tip current caused by H_2 bubbles.[211] Finally, it was concluded that tensile strain stimulates the kinetics of hydrogen evolution in S-vacancies in MoS_2.[211]

Very recently, a thorough investigation of HER electroactivity in MoS_2 was done by Sun *et al.*[45] through nanoscale mapping with <20 nm spatial resolution. The HER activity of metallic (1T) and semiconducting (2H) phases within the MoS_2 nanostructure was compared by employing SECM in SG/TC mode, in which case it was found that the metallic phase has superior HER activity compared to 2H, while within the 2H phase, the edges have higher activity (Fig. 24). These results might be an

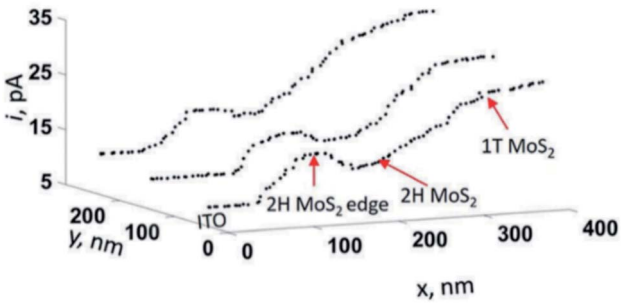

Fig. 24 Line profiles of the hydrogen evolution reaction obtained by using SECM in SG/TC mode in mixed-phase MoS_2 nanosheets. Reproduced from ref. 45 with permission from the Royal Society of Chemistry © 2019.

Open Access Article. Published on 19 November 2020. Downloaded on 4/20/2026 1:55:05 AM.
This article is licensed under a Creative Commons Attribution-NonCommercial 3.0 Unported Licence.

important indication for converting MoS_2 into an only-metallic phase for an elevated HER activity.[45]

An improvement in MoS_2 activity can be obtained by incorporating it into matrices with high conductivity.[213] This was done by Kumar *et al.*[214] who combined MoS_2 NPs of the T1 phase with graphene oxide (GO) or reduced graphene oxide (rGO) in which case both composites exhibited comparable HER activity to the state-of-the-art Pt/C.[214]

On the other hand, nickel foams with a karst landform structure were studied for their HER activity by Gao *et al.*[215] through SG/TC mode, a Pt nanoelectrode and Si substrate. The SECM images indicate a high activity in the valley areas, which was confirmed by the topographical image as well.[215] The same electrocatalyst exhibited good activity towards the OER as well and this performance is attributed to the karst landform structure, which seems to ease the mass diffusion and to provide sufficient catalytic sites.[215]

SECM was employed as well for the investigation of photogenerated hydrogen at a 1,2-dichloroethane/water (DCE/W) interface by Jedraszko *et al.*[216] During the HER, decamethylruthenocene (DMRc) is formed as a by-product during the hydrogen evolution, and then serves as an electron donor, which permits a continuous HER.[216] The SECM setup consisted of two Pt electrodes separated by only 50 μm from each other through a liquid/liquid interface, in order to ensure an efficient generation of DMRc by $DMRc^+$ reduction. Close to the DCE/W interface, the bottom electrode served for uninterrupted regeneration of $DMRc^+$, while the photogenerated hydrogen was captured at the upper electrode. Herein, SECM was used to demonstrate the regeneration of DMRs, which opens the possibilities for further development of biphasic systems towards H_2 generation. The experimental details and the resulting tip current due to H_2 oxidation in the presence and absence of light can be seen in Fig. 25.

Bentley and Unwin[217] demonstrated through studying the HER at MoS_2 how SECCM is a powerful robust tool that can be used to obtain topographical and voltammetric data at a 50 nm spatial resolution, and potential-resolved movies of electrocatalytic performance, in just minutes. The working principle of this technique is illustrated in Fig. 26. The authors were able to obtain the specificities of the catalyst surface at a sub-10 nm scale. Moreover, {111} Au nanocrystals (AuNCs) were also investigated, displaying uniform HER activity up to a sub-single entity level.

Choi *et al.*[218] took advantage of SECCM for evaluating the HER electrocatalytic activity of individual Au nanocubes (NCs, {100}) and nano-octahedra (ODs, {111}) both with edge lengths <100 nm, by using a dual barrel nanopipette (~200 nm in outer diameter) and glassy carbon as a substrate. The authors established that performing CV through SECCM is an efficient way to investigate the HER activity of individual nanoparticles. The current results showed that the cubes have a higher performance compared to the octahedra and misshaped particles, a result which matched the macroscale measurements. This outcome may be valuable when it comes to effective future design of HER electrocatalysts.

A metal free material that has been studied for HER activity is also hexagonal boron nitride (h-BN), thanks to the possibility of electronic tunneling[219] between its ultrathin layers and the underlying metal support substrate.[220] The effect of a metal substrate on the electrocatalytic activity of 2D h-BN nanosheets was studied through SECCM in hopping mode by Liu *et al.*[221] The authors investigated the grown h-BN nanosheets on Cu and on Au substrates, namely h-BN/Cu and h-BN/Au, respectively, by using a 0.1 M $HClO_4$ filled nanopipette with a diameter from 150 to 300 nm. The exchange current evaluated by local voltammetry and Tafel analysis showed that h-BN/Au has superior

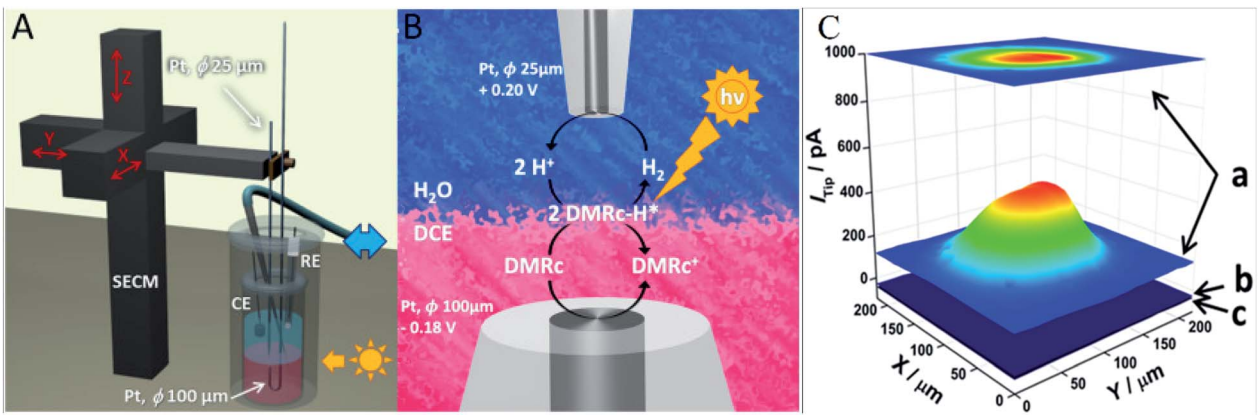

Fig. 25 (A) Schematic representation of the used SECM setup for the study of DMRc regeneration with two Pt microelectrodes placed near immiscible electrolyte solutions (ITIES), where the blue double arrow represents the connection to the syringe pump that controls the position of the liquid/liquid interface. Anaerobic conditions are supplied by Ar, (B) schematic representation of the reaction and (C) current of the tip measured at 0.20 V *vs.* RHE, above the bottom Pt electrode and polarized at −0.18 V (a) exposed to UV light, (b) in darkness and (c) in darkness without substrate polarization. The organic phase contained 5 mmol dm^{-3} DMRc and 5 mmol dm^{-3} bis(triphenylphosphoranylidene)ammonium tetrakis(pentafluorophenyl)borate (BATB). The solution in which the Pt tip was immersed contained 0.1 M $HClO_4$ and 5 mM lithium tetrakis(-pentafluorophenyl)borate (LiTB). The distance between the microelectrodes was 50 μm and the tip lateral velocity was 50 μm s^{-1} Reproduced from ref. 216 with permission from Elsevier © 2018.

© 2021 The Author(s). Published by the Royal Society of Chemistry

Open Access Article. Published on 19 November 2020. Downloaded on 4/20/2026 1:55:05 AM.
This article is licensed under a Creative Commons Attribution-NonCommercial 3.0 Unported Licence.

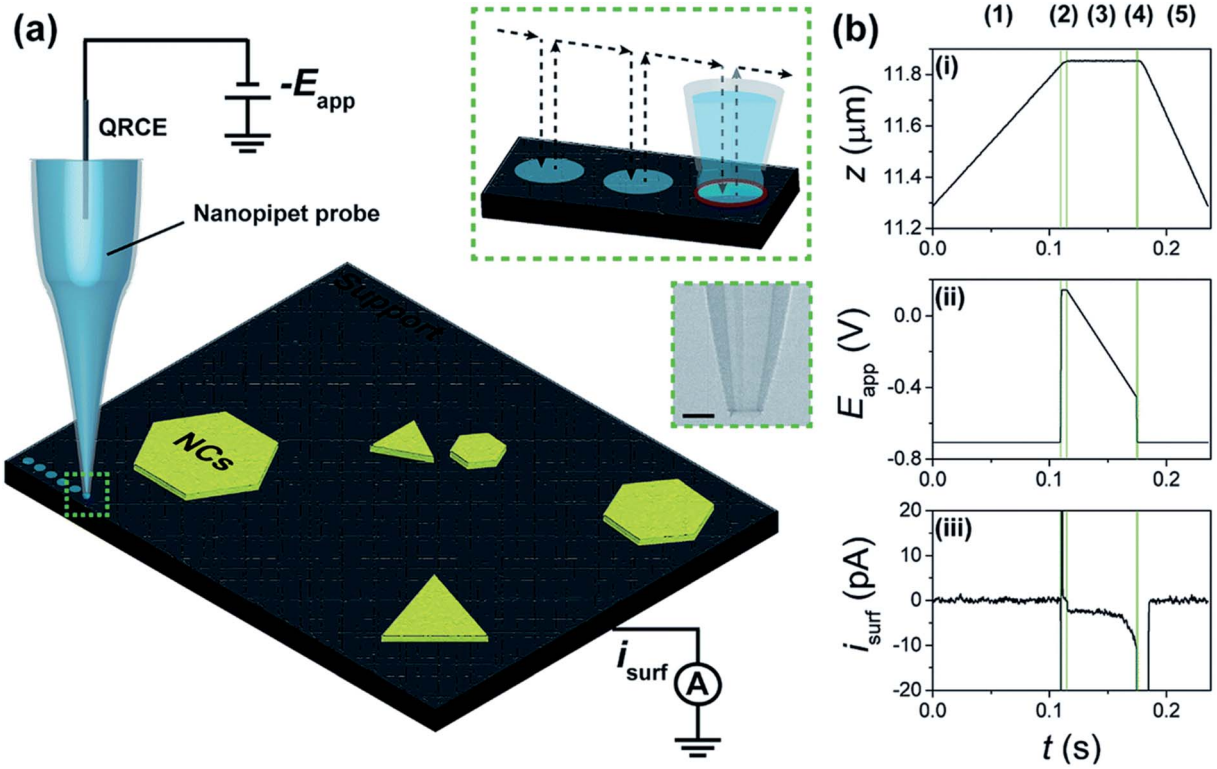

Fig. 26 (a) Scheme of a nanoscale synchronous electrochemical/topographical map obtained by SECCM in voltammetric hopping mode by using a single channel nanopipette containing 100 mM H_2SO_4 and a GC support. The voltage was applied at the QRCE to control the WE potential (E_{app}) while the WE current (i_{surf}) was measured. The latter also served as a feedback signal for detecting meniscus-surface contact during the approach. Arrows show the movement of the nanopipette probe along the surface during scanning (inset, top-right). (b) Plots of (i) z-extension, (ii) E_{app} and (iii) i_{surf} during a 'single hop' at the AuNC substrate. Scan rate (v) = 10 V s^{-1} and data acquisition time (t_d) = 260 μs. Reproduced from ref. 217 with permission from the Royal Society of Chemistry © 2018.

HER electrocatalytic activity, easing the way to a proper future design of HER electrocatalysts.

Emerging topics

The electrochemical reduction of the greenhouse gas CO_2 has attracted attention lately,[222] since it can lead to the formation of beneficial chemicals.[223–225] Some products that form during the CO_2RR can be evaluated through the RRDE method;[226–228] however a better collection efficiency may be achieved by SECM.[229]

The catalytic properties of boron-doped graphene (BG) for the reduction of CO_2 to formate (FA) were studied by Sreekanth *et al.*[230] SECM in SG/TC mode was utilized for identifying the electroactive product (FA) through a Pt UME, that forms during CO_2 reduction in the GCE substrate in 0.1 M $KHCO_3$. The oxidation of FA was spotted through cyclic voltammetry, with a sharp tip current peak at a substrate potential of −1.4 V *vs.* SCE. Control experiments were conducted to ensure that the signal is associated with the FA oxidation and not with CO oxidation as another potential product. Finally, the BG catalyst exhibited higher tip current during FA oxidation compared to the benchmark catalyst (Bi).[230,231] The same group investigated the formation of CO and FA through bicarbonate reduction with SECM in SG/TC mode.[229] Moreover, the good catalytic activity of silver nanoparticles and nanoclusters (Ag NPs and Ag NCs respectively) for bicarbonate reduction to FA was demonstrated by Arrocha-Arcos *et al.*[232] by using SG/TC mode of SECM.

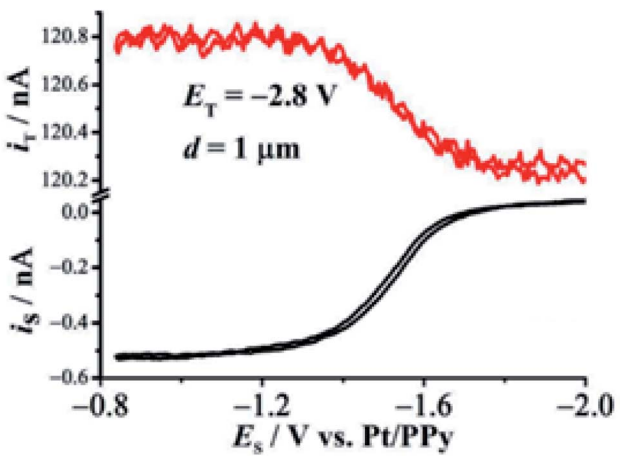

Fig. 27 The black curve represents the current due to $CO_2^{\bullet-}$ collection at the SECM substrate (an a = 12.5 μm Au UME) in DMF which contains 0.1 M $TBAPF_6$. The tip potential was kept at E_t = −2.8 V, while the substrate potential was swept from −2.1 V to −0.9 V. The tip current is represented by the red curve. Reproduced from ref. 46 with permission from the American Chemical Society © 2017.

Open Access Article. Published on 19 November 2020. Downloaded on 4/20/2026 1:55:05 AM.
This article is licensed under a Creative Commons Attribution-NonCommercial 3.0 Unported Licence.

The first step of CO_2 reduction is the one-electron transfer reaction of $CO_2^{\bullet-}$ production, an intermediate which has a very short lifetime[46] as it can be quickly protonated, dimerized, or reduced.[233] Therefore, it has been a major challenge to capture it experimentally, leading to a lack of understanding of the overall CO_2RR mechanism. Not long ago, this has been achieved by Kai *et al.*,[46] who detected for the first time the $CO_2^{\bullet-}$ intermediate through SECM in TG/SC mode, by making use of an Hg/Pt UME tip and small distances between the tip and the substrate (Au UME). The substrate current rose due to intermediate detection and the tip current increased due to the oxidation of some $CO_2^{\bullet-}$ to CO_2 at the sample which is fed back to the tip[46] (Fig. 27).

Grain boundaries (GBs) in polycrystalline materials have been shown to have an effect on CO_2RR electrocatalysis;[234,235] however for a proper future design, a thorough understanding of the GB dependence in activity is necessary. Mariano *et al.*[236] have studied the influence of GB on polycrystalline Au with big grain sizes on the CO_2RR to CO. The authors used a ~300 nm single-barrel pipette in hopping mode, by applying a fixed potential at the Au substrate. Current is recorded when the droplet contacts the sample, and then the pipette is moved away for the next measurement, allowing the recording of line scans. Through bulk electrochemistry the authors found that the CO_2RR increases with the density of GBs, while SECCM was used to justify this result, in which case it was found that surface terminations are responsible for the elevated CO_2RR (Fig. 28).

Nanoscale measurements can be helpful in cases when one needs to discriminate between the performance of an ensemble with that of individual nanoparticles.[237] Such measurements were done by Kim *et al.*[43] for the study of the hydrogen oxidation

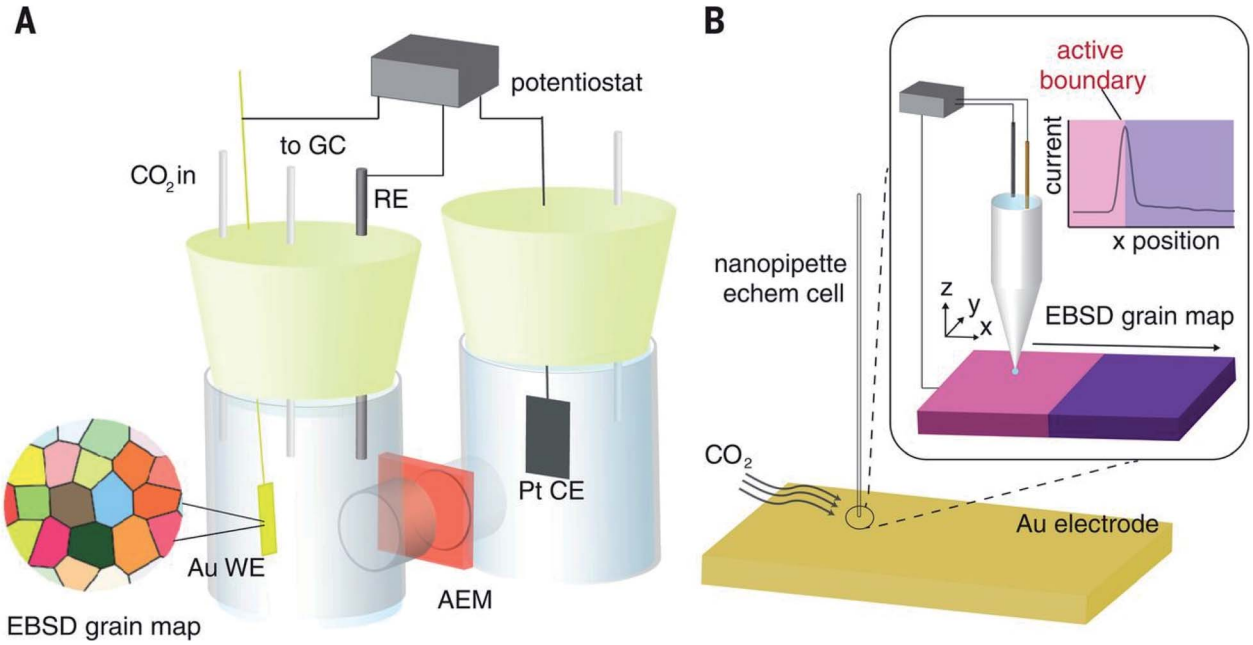

Fig. 28 Two approaches detailed in this work for the electrochemical characterization of defect effects on the CO_2RR. (A) Bulk electrolysis of a well-defined polycrystalline Au electrode within a glass, two-compartment H cell and (B) SECCM using a ~300 nm nanopipette electrochemical cell. Reproduced from ref. 236 with permission from the American Association for the Advancement of Science © 2017.

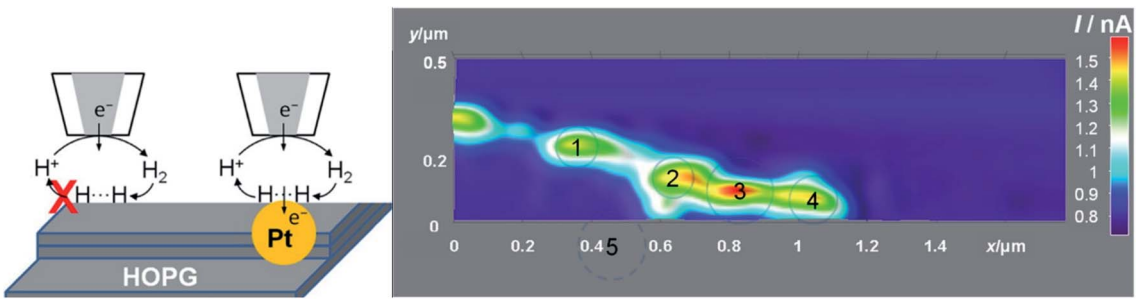

Fig. 29 (left) Schematic representation of the electron transfer reactions in the substrate and sample by means of SECM and (right) SECM image of the electron transfer reaction of H^+/H at five Pt nanoparticles in 2 mM $HClO_4$ and 10 mM $NaClO_4$ with the tip polarized at −1.0 V and the substrate at −0.4 V *vs.* a Pt quasi reference electrode (QRE). Pt nanotip was scanned at 200 nm s^{-1}. Reproduced with permission from ref. 43 © 2016 American Chemical Society.

© 2021 The Author(s). Published by the Royal Society of Chemistry

Open Access Article. Published on 19 November 2020. Downloaded on 4/20/2026 1:55:05 AM.
This article is licensed under a Creative Commons Attribution-NonCommercial 3.0 Unported Licence.

reaction (HOR) of Pt NPs electrodeposited on highly oriented pyrolytic graphite (HOPG), with a Pt nanoelectrode at d = 134 nm. To acquire the SECM images, H^+ got reduced at the tip, while the H_2 which was formed afterwards got oxidized at the sample (Fig. 29 left). In Fig. 29 (right) one can see the current of H_2 oxidation at five distinct nanoparticles. Furthermore, as a result of elevated mass transfer due to nano-scale conditions, a HOR rate constant of $k^0_{\text{eff}} \geq 2$ cm s^{-1} was acquired.[43]

Conclusion and prospects

In this review we summarized recent investigations (mostly between 2015–2020) made for the ORR, OER and HER electrocatalysts, by employing SECM and other related techniques. The non-noble class of materials that seem to be frequently studied for the two former reactions are metal oxides on carbon supports, in which case the synergetic effects between the two components can lead to a superior electrocatalytic activity. As for the HER, metal sulfides seem to have attention as promising non-noble electrocatalysts. Generally, the local ORR activity was studied in RC-SECM mode and then compared to the RDE results. However, in some cases, the intermediate produced was quantified as well by SECM, where a combination of RC and generation/collection modes was used (pulsed profile). This approach, which allows the calculation of n, is not put into practice as much as one would have expected. Instead, the selectivity is mostly acquired from RDE and/or RRDE methods, and then the activity is somewhat qualitatively compared to RC-SECM results. The outcome of the different approaches is not always concordant, and thus additional research should be a prerequisite for more unambiguous conclusions regarding their compatibility and complementarity.

The gas-evolution reactions (OER and HER) are studied essentially in SG/TC mode. SI-SECM seems to have potential in the study of the OER, especially for mechanistic studies while Raman-SECM was used for OER *in situ* studies. Concerning the experimental conditions for all reactions, interestingly a Pt UME of 25 μm diameter was most frequently used, along with mainly an ITO or GCE substrate, at different tip-to-substrate distances. Since most experiments were performed in alkaline electrolytes, it would be interesting for further studies to conduct more experiments in acidic media, as it would expand the application possibilities in different kinds of fuel cells. The combined techniques such as SECM-AFM and SECM-SICM were utilized for ORR investigations, while SECCM found most utility in the analysis of the HER. Finally, the study of the CO_2RR with SECM seems to be auspicious, while further SPM investigations of the HOR, especially in non-noble electrocatalysis, are highly encouraged. Clearly, SECM appears to be the leader within the SPM techniques for electrocatalytic investigations.

Conflicts of interest

There are no conflicts to declare.

Acknowledgements

The authors acknowledge the SENTINEL project, funded by the European Union's Horizon 2020 Research and Innovation Program under the Marie Skłodowska-Curie grant agreement no. 812398, and the PEGASUS project, funded by the European Union's Horizon 2020 Research and Innovation Program FCH-01-2-2017, no. 779550.

References

1 F. Perera, *Int. J. Environ. Res. Public Health*, 2017, **15**, 16.
2 H. B. Gray, *Nat. Chem.*, 2009, **1**, 7.
3 T. R. Cook, D. K. Dogutan, S. Y. Reece, Y. Surendranath, T. S. Teets and D. G. Nocera, *Chem. Rev.*, 2010, **110**, 6474–6502.
4 P. A. Owusu and S. Asumadu-Sarkodie, *Cogent Eng.*, 2016, **3**, 1167990.
5 L. Carrette, K. A. Friedrich and U. Stimming, *Fuel Cells*, 2001, **1**, 5–39.
6 A. Mikolajczuk-Zychora, A. Borodzinski, P. Kedzierzawski, B. Mierzwa, M. Mazurkiewicz-Pawlicka, L. Stobinski, E. Ciecierska, A. Zimoch and M. Opałło, *Appl. Surf. Sci.*, 2016, **388**, 645–652.
7 L. Aguilar, S. Zha, Z. Cheng, J. Winnick and M. Liu, *J. Power Sources*, 2004, **135**, 17–24.
8 A. Serov and C. Kwak, *Appl. Catal., B*, 2010, **98**, 1–9.
9 C. Lamy, S. Rousseau, E. M. Belgsir, C. Coutanceau and J.-M. Léger, *Electrochim. Acta*, 2004, **49**, 3901–3908.
10 S. Wasmus and A. Küver, *J. Electroanal. Chem.*, 1999, **461**, 14–31.
11 A. Afif, N. Radenahmad, Q. Cheok, S. Shams, J. H. Kim and A. K. Azad, *Renewable Sustainable Energy Rev.*, 2016, **60**, 822–835.
12 C. Thomas, *Int. J. Hydrogen Energy*, 1998, **23**, 507–516.
13 C. G. Morales-Guio, L.-A. Stern and X. Hu, *Chem. Soc. Rev.*, 2014, **43**, 6555.
14 J. O. M. Bockris, *Int. J. Hydrogen Energy*, 2013, **38**, 2579–2588.
15 E. S. Hanley, J. Deane and B. Ó. Gallachóir, *Renewable Sustainable Energy Rev.*, 2018, **82**, 3027–3045.
16 Y. Jiao, Y. Zheng, M. Jaroniec and S. Z. Qiao, *Chem. Soc. Rev.*, 2015, **44**, 2060–2086.
17 J. A. Turner, *Science*, 2004, **305**, 972–974.
18 C. Freire, D. M. Fernandes, M. Nunes and V. K. Abdelkader, *ChemCatChem*, 2018, **10**, 1703–1730.
19 A. Aijaz, J. Masa, C. Rösler, W. Xia, P. Weide, A. J. R. Botz, R. A. Fischer, W. Schuhmann and M. Muhler, *Angew. Chem., Int. Ed.*, 2016, **55**, 4087–4091.
20 F.-Y. Yu, Z.-L. Lang, L.-Y. Yin, K. Feng, Y.-J. Xia, H.-Q. Tan, H.-T. Zhu, J. Zhong, Z.-H. Kang and Y.-G. Li, *Nat. Commun.*, 2020, **11**, 490.
21 E. S. Davydova, S. Mukerjee, F. Jaouen and D. R. Dekel, *ACS Catal.*, 2018, **8**, 6665–6690.
22 Y. Lee, J. Suntivich, K. J. May, E. E. Perry and Y. Shao-Horn, *J. Phys. Chem. Lett.*, 2012, **3**, 399–404.

Open Access Article. Published on 19 November 2020. Downloaded on 4/20/2026 1:55:05 AM.
This article is licensed under a Creative Commons Attribution-NonCommercial 3.0 Unported Licence.

23 O. Schmidt, A. Gambhir, I. Staffell, A. Hawkes, J. Nelson and S. Few, *Int. J. Hydrogen Energy*, 2017, **42**, 30470–30492.
24 G. J. Offer, D. Howey, M. Contestabile, R. Clague and N. P. Brandon, *Energy Policy*, 2010, **38**, 24–29.
25 J. Wang, H. Wang and Y. Fan, *Engineering*, 2018, **4**, 352–360.
26 Y. Wang, D. F. Ruiz Diaz, K. S. Chen, Z. Wang and X. C. Adroher, *Mater. Today*, 2020, **32**, 178–203.
27 M. M. Whiston, I. L. Azevedo, S. Litster, K. S. Whitefoot, C. Samaras and J. F. Whitacre, *Proc. Natl. Acad. Sci. U. S. A.*, 2019, **116**, 4899–4904.
28 P. Bertoncello, *Energy Environ. Sci.*, 2010, **3**, 1620.
29 D. Polcari, P. Dauphin-Ducharme and J. Mauzeroll, *Chem. Rev.*, 2016, **116**, 13234–13278.
30 Z. Jia, G. Yin and J. Zhang, in *Rotating Electrode Methods and Oxygen Reduction Electrocatalysts*, Elsevier, 2014, pp. 199–229.
31 *Rotating electrode methods and oxygen reduction electrocatalysts*, ed. W. Xing, G. Yin and J. Zhang, Elsevier, Amsterdam, 2014.
32 C. Du, Q. Tan, G. Yin and J. Zhang, in *Rotating Electrode Methods and Oxygen Reduction Electrocatalysts*, Elsevier, 2014, pp. 171–198.
33 S. M. Salapaka and M. V. Salapaka, *IEEE Contr. Syst.*, 2008, **28**, 65–83.
34 C. G. Zoski, *J. Electrochem. Soc.*, 2016, **163**, H3088–H3100.
35 S. C. S. Lai, J. V. Macpherson and P. R. Unwin, *MRS Bull.*, 2012, **37**, 668–674.
36 *Scanning electrochemical microscopy*, ed. A. J. Bard and M. V. Mirkin, CRC Press, Boca Raton, Fla, 2nd edn, 2012.
37 R. Cornut, M. Mayoral, D. Fabre and J. Mauzeroll, *J. Electrochem. Soc.*, 2010, **157**, F77.
38 R. Cornut, S. Poirier and J. Mauzeroll, *Anal. Chem.*, 2012, **84**, 3531–3537.
39 E. Ventosa and W. Schuhmann, *Phys. Chem. Chem. Phys.*, 2015, **17**, 28441–28450.
40 J. Heinze, *Angew. Chem., Int. Ed. Engl.*, 1993, **32**, 1268–1288.
41 R. Senthamarai and L. Rajendran, *J. Theor. Comput. Chem.*, 2008, **07**, 205–219.
42 W. Schuhmann and M. Bron, in *Polymer Electrolyte Membrane and Direct Methanol Fuel Cell Technology*, Elsevier, 2012, pp. 399–424.
43 J. Kim, C. Renault, N. Nioradze, N. Arroyo-Currás, K. C. Leonard and A. J. Bard, *J. Am. Chem. Soc.*, 2016, **138**, 8560–8568.
44 T. Kai, C. G. Zoski and A. J. Bard, *Chem. Commun.*, 2018, **54**, 1934–1947.
45 T. Sun, H. Zhang, X. Wang, J. Liu, C. Xiao, S. U. Nanayakkara, J. L. Blackburn, M. V. Mirkin and E. M. Miller, *Nanoscale Horiz.*, 2019, **4**, 619–624.
46 T. Kai, M. Zhou, Z. Duan, G. A. Henkelman and A. J. Bard, *J. Am. Chem. Soc.*, 2017, **139**, 18552–18557.
47 I. Liberman, W. He, R. Shimoni, R. Ifraemov and I. Hod, *Chem. Sci.*, 2020, **11**, 180–185.
48 H. S. Ahn and A. J. Bard, *J. Am. Chem. Soc.*, 2015, **137**, 612–615.
49 A. Davoodi, J. Pan, C. Leygraf and S. Norgren, *Appl. Surf. Sci.*, 2006, **252**, 5499–5503.
50 J. Zhang, C. J. Slevin, C. Morton, P. Scott, D. J. Walton and P. R. Unwin, *J. Phys. Chem. B*, 2001, **105**, 11120–11130.
51 M. Tavakkoli, E. Flahaut, P. Peljo, J. Sainio, F. Davodi, E. V. Lobiak, K. Mustonen and E. I. Kauppinen, *ACS Catal.*, 2020, **10**, 4647–4658.
52 G. Zampardi, E. Ventosa, F. La Mantia and W. Schuhmann, *Chem. Commun.*, 2013, **49**, 9347.
53 A. Dobrzeniecka, A. Zeradjanin, J. Masa, A. Puschhof, J. Stroka, P. J. Kulesza and W. Schuhmann, *Catal. Today*, 2013, **202**, 55–62.
54 I. Hijazi, T. Bourgeteau, R. Cornut, A. Morozan, A. Filoramo, J. Leroy, V. Derycke, B. Jousselme and S. Campidelli, *J. Am. Chem. Soc.*, 2014, **136**, 6348–6354.
55 A. Maljusch, E. Ventosa, R. A. Rincón, A. S. Bandarenka and W. Schuhmann, *Electrochem. Commun.*, 2014, **38**, 142–145.
56 X. Chen, A. J. R. Botz, J. Masa and W. Schuhmann, *J. Solid State Electrochem.*, 2016, **20**, 1019–1027.
57 A. Jindal, S. Basu and C. P. Aby, *RSC Adv.*, 2015, **5**, 69378–69387.
58 O. Sklyar and G. Wittstock, *J. Phys. Chem. B*, 2002, **106**, 7499–7508.
59 M. Ludwig, C. Kranz, W. Schuhmann and H. E. Gaub, *Rev. Sci. Instrum.*, 1995, **66**, 2857–2860.
60 K. Mkelvey, M. A. Edwards and P. R. Unwin, *Anal. Chem.*, 2010, **82**, 6334–6337.
61 R. A. Lazenby, K. MKelvey and P. R. Unwin, *Anal. Chem.*, 2013, **85**, 2937–2944.
62 M. Gębala, W. Schuhmann and F. La Mantia, *Electrochem. Commun.*, 2011, **13**, 689–693.
63 N. Ebejer, A. G. Güell, S. C. S. Lai, K. McKelvey, M. E. Snowden and P. R. Unwin, *Annu. Rev. Anal. Chem.*, 2013, **6**, 329–351.
64 A. J. Bard, F. R. F. Fan, J. Kwak and O. Lev, *Anal. Chem.*, 1989, **61**, 132–138.
65 Y. Shao and M. V. Mirkin, *J. Phys. Chem. B*, 1998, **102**, 9915–9921.
66 J. V. Macpherson and P. R. Unwin, *Anal. Chem.*, 2000, **72**, 276–285.
67 B. B. Katemann and W. Schuhmann, *Electroanalysis*, 2002, **14**, 22–28.
68 K. Eckhard, X. Chen, F. Turcu and W. Schuhmann, *Phys. Chem. Chem. Phys.*, 2006, **8**, 5359.
69 N. A. Payne, L. I. Stephens and J. Mauzeroll, *Corrosion*, 2017, **73**, 759–780.
70 S. Bergner, P. Vatsyayan and F.-M. Matysik, *Anal. Chim. Acta*, 2013, **775**, 1–13.
71 S. Amemiya, A. J. Bard, F.-R. F. Fan, M. V. Mirkin and P. R. Unwin, *Annu. Rev. Anal. Chem.*, 2008, **1**, 95–131.
72 A. R. Kucernak, P. B. Chowdhury, C. P. Wilde, G. H. Kelsall, Y. Y. Zhu and D. E. Williams, *Electrochim. Acta*, 2000, **45**, 4483–4491.
73 K. C. Leonard and A. J. Bard, *J. Am. Chem. Soc.*, 2013, **135**, 15890–15896.
74 J. Rodríguez-López, M. A. Alpuche-Avilés and A. J. Bard, *J. Am. Chem. Soc.*, 2008, **130**, 16985–16995.
75 P. Hansma, B. Drake, O. Marti, S. Gould and C. Prater, *Science*, 1989, **243**, 641–643.

© 2021 The Author(s). Published by the Royal Society of Chemistry

Open Access Article. Published on 19 November 2020. Downloaded on 4/20/2026 1:55:05 AM.
This article is licensed under a Creative Commons Attribution-NonCommercial 3.0 Unported Licence.

76 C.-C. Chen, Y. Zhou and L. A. Baker, *Annu. Rev. Anal. Chem.*, 2012, **5**, 207–228.
77 A. Page, D. Perry and P. R. Unwin, *Proc. R. Soc. A*, 2017, **473**, 20160889.
78 D. Momotenko, K. McKelvey, M. Kang, G. N. Meloni and P. R. Unwin, *Anal. Chem.*, 2016, **88**, 2838–2846.
79 N. A. Payne, J. I. G. Dawkins, S. B. Schougaard and J. Mauzeroll, *Anal. Chem.*, 2019, **91**, 15718–15725.
80 V. Shkirskiy, M. Kang, I. J. McPherson, C. L. Bentley, O. J. Wahab, E. Daviddi, A. W. Colburn and P. R. Unwin, *Anal. Chem.*, 2020, **92**, 12509–12517.
81 C.-C. Chen, Y. Zhou and L. A. Baker, *Annu. Rev. Anal. Chem.*, 2012, **5**, 207–228.
82 J. Zhang, T. Zhu, J. Lang, W. Fu and F. Li, *Curr. Opin. Electrochem.*, 2020, **22**, 178–185.
83 X. Shi, W. Qing, T. Marhaba and W. Zhang, *Electrochim. Acta*, 2020, **332**, 135472.
84 C. L. Bentley, J. Edmondson, G. N. Meloni, D. Perry, V. Shkirskiy and P. R. Unwin, *Anal. Chem.*, 2019, **91**, 84–108.
85 N. Ebejer, M. Schnippering, A. W. Colburn, M. A. Edwards and P. R. Unwin, *Anal. Chem.*, 2010, **82**, 9141–9145.
86 N. Ebejer, A. G. Güell, S. C. S. Lai, K. McKelvey, M. E. Snowden and P. R. Unwin, *Annu. Rev. Anal. Chem.*, 2013, **6**, 329–351.
87 H. V. Patten, S. C. S. Lai, J. V. Macpherson and P. R. Unwin, *Anal. Chem.*, 2012, **84**, 5427–5432.
88 K. McKelvey, M. A. O'Connell and P. R. Unwin, *Chem. Commun.*, 2013, **49**, 2986.
89 H. V. Patten, K. E. Meadows, L. A. Hutton, J. G. Iacobini, D. Battistel, K. McKelvey, A. W. Colburn, M. E. Newton, J. V. Macpherson and P. R. Unwin, *Angew. Chem., Int. Ed.*, 2012, **51**, 7002–7006.
90 T. S. Miller, N. Ebejer, A. G. Güell, J. V. Macpherson and P. R. Unwin, *Chem. Commun.*, 2012, **48**, 7435.
91 B. Liu, Y. Shao and M. V. Mirkin, *Anal. Chem.*, 2000, **72**, 510–519.
92 S. E. F. Kleijn, S. C. S. Lai, T. S. Miller, A. I. Yanson, M. T. M. Koper and P. R. Unwin, *J. Am. Chem. Soc.*, 2012, **134**, 18558–18561.
93 D. Momotenko, J. C. Byers, K. McKelvey, M. Kang and P. R. Unwin, *ACS Nano*, 2015, **9**, 8942–8952.
94 C. L. Bentley, M. Kang and P. R. Unwin, *Curr. Opin. Electrochem.*, 2017, **6**, 23–30.
95 O. J. Wahab, M. Kang and P. R. Unwin, *Curr. Opin. Electrochem.*, 2020, **22**, 120–128.
96 J. L. Toca-Herrera, *ChemSusChem*, 2019, **12**, 603–611.
97 G. Haugstad, *Atomic Force Microscopy: Understanding Basic Modes and Advanced Applications*, Wiley, 2012.
98 Y. F. Dufrêne, T. Ando, R. Garcia, D. Alsteens, D. Martinez-Martin, A. Engel, C. Gerber and D. J. Müller, *Nat. Nanotechnol.*, 2017, **12**, 295–307.
99 X. Deng, F. Xiong, X. Li, B. Xiang, Z. Li, X. Wu, C. Guo, X. Li, Y. Li, G. Li, W. Xiong and Z. Zeng, *J. Nanobiotechnol.*, 2018, **16**, 102.
100 M. R. Nellist, F. A. L. Laskowski, J. Qiu, H. Hajibabaei, K. Sivula, T. W. Hamann and S. W. Boettcher, *Nat. Energy*, 2018, **3**, 46–52.
101 N. Pavliček and L. Gross, *Nat. Rev. Chem.*, 2017, **1**, 0005.
102 Y. Xing, M. Xu, X. Gui, Y. Cao, B. Babel, M. Rudolph, S. Weber, M. Kappl and H.-J. Butt, *Adv. Colloid Interface Sci.*, 2018, **256**, 373–392.
103 I. W. Rangelow, M. Kaestner, T. Ivanov, A. Ahmad, S. Lenk, C. Lenk, E. Guliyev, A. Reum, M. Hofmann, C. Reuter and M. Holz, *J. Vac. Sci. Technol., B: Nanotechnol. Microelectron.: Mater., Process., Meas., Phenom.*, 2018, **36**, 06J102.
104 N. Balke, D. Bonnell, D. S. Ginger and M. Kemerink, *MRS Bull.*, 2012, **37**, 633–637.
105 S. Sadewasser and C. Barth, in *Characterization of Materials*, ed. E. N. Kaufmann, John Wiley & Sons, Inc., Hoboken, NJ, USA, 2012.
106 D. S. Jakob, H. Wang and X. G. Xu, *ACS Nano*, 2020, **14**, 4839–4848.
107 S. Jesse, A. Kumar, T. M. Arruda, Y. Kim, S. V. Kalinin and F. Ciucci, *MRS Bull.*, 2012, **37**, 651–658.
108 J. Iturri and J. Toca-Herrera, *Polymers*, 2017, **9**, 383.
109 L. Khotseng, in *Electrocatalysts for Fuel Cells and Hydrogen Evolution - Theory to Design*, ed. A. Ray, I. Mukhopadhyay and R. K. Pati, IntechOpen, 2018.
110 Y. Nie, L. Li and Z. Wei, *Chem. Soc. Rev.*, 2015, **44**, 2168–2201.
111 S. Gao, H. Fan and S. Zhang, *J. Mater. Chem. A*, 2014, **2**, 18263–18270.
112 A. Dobrzeniecka, A. R. Zeradjanin, J. Masa, M. Blicharska, D. Wintrich, P. J. Kulesza and W. Schuhmann, *Catal. Today*, 2016, **262**, 74–81.
113 A. A. Gewirth and M. S. Thorum, *Inorg. Chem.*, 2010, **49**, 3557–3566.
114 N. Muthuswamy, M. E. M. Buan, J. C. Walmsley and M. Rønning, *Catal. Today*, 2018, **301**, 11–16.
115 J. L. Fernández and A. J. Bard, *Anal. Chem.*, 2004, **76**, 2281–2289.
116 C. M. Sánchez-Sánchez and A. J. Bard, *Anal. Chem.*, 2009, **81**, 8094–8100.
117 K. Eckhard and W. Schuhmann, *Electrochim. Acta*, 2007, **53**, 1164–1169.
118 M. Shao, P. Liu, J. Zhang and R. Adzic, *J. Phys. Chem. B*, 2007, **111**, 6772–6775.
119 J. V. Perales-Rondón, E. Herrero, J. Solla-Gullón, C. M. Sánchez-Sánchez and V. Vivier, *J. Electroanal. Chem.*, 2017, **793**, 218–225.
120 J. L. Fernández, K. P. Imaduwage and C. G. Zoski, *Electrochim. Acta*, 2015, **180**, 460–470.
121 Y. Zhang, X. Wu, Y. Fu, W. Shen, X. Zeng and W. Ding, *J. Mater. Res.*, 2014, **29**, 2863–2870.
122 Y.-B. Cho, C. Lee and Y. Lee, *J. Electrochem. Soc.*, 2015, **162**, H792–H798.
123 A. Botz, J. Clausmeyer, D. Öhl, T. Tarnev, D. Franzen, T. Turek and W. Schuhmann, *Angew. Chem., Int. Ed.*, 2018, **57**, 12285–12289.
124 W. Li, F.-R. F. Fan and A. J. Bard, *J. Solid State Electrochem.*, 2012, **16**, 2563–2568.

© 2021 The Author(s). Published by the Royal Society of Chemistry

Open Access Article. Published on 19 November 2020. Downloaded on 4/20/2026 1:55:05 AM.
This article is licensed under a Creative Commons Attribution-NonCommercial 3.0 Unported Licence.

125 J. K. Nørskov, J. Rossmeisl, A. Logadottir, L. Lindqvist, J. R. Kitchin, T. Bligaard and H. Jónsson, *J. Phys. Chem. B*, 2004, **108**, 17886–17892.
126 X. Sun, W. Li, H. Mi, Y. Li, P. Zhang and X. Ren, *Int. J. Hydrogen Energy*, 2018, **43**, 5530–5540.
127 T. N. Pham Truong, H. Randriamahazaka and J. Ghilane, *ACS Catal.*, 2018, **8**, 869–875.
128 S. Kim, S.-C. Lee, C. Lee, M. H. Kim and Y. Lee, *Nano Energy*, 2018, **48**, 134–143.
129 V. Singh, A. Tiwari and T. C. Nagaiah, *J. Mater. Chem. A*, 2018, **6**, 22545–22554.
130 J. Xiao, Q. Kuang, S. Yang, F. Xiao, S. Wang and L. Guo, *Sci. Rep.*, 2013, **3**, 2300.
131 H. Liu, X. Zhu, M. Li, Q. Tang, G. Sun and W. Yang, *Electrochim. Acta*, 2014, **144**, 31–41.
132 A. Tiwari, V. Singh and T. C. Nagaiah, *J. Mater. Chem. A*, 2018, **6**, 2681–2692.
133 B. Sidhureddy, S. Prins, J. Wen, A. R. Thiruppathi, M. Govindhan and A. Chen, *ACS Appl. Mater. Interfaces*, 2019, **11**, 18295–18304.
134 X. Yan, K. Li, L. Lyu, F. Song, J. He, D. Niu, L. Liu, X. Hu and X. Chen, *ACS Appl. Mater. Interfaces*, 2016, **8**, 3208–3214.
135 F. Zheng, D. Zhu and Q. Chen, *ACS Appl. Mater. Interfaces*, 2014, **6**, 9256–9264.
136 M. Michalak, A. Roguska, W. Nogala and M. Opallo, *Nanoscale Adv.*, 2019, **1**, 2645–2653.
137 Q. Zhang, P. Liu, Z. Zhu, J. Zhang and F. Cao, *Corros. Sci.*, 2020, **164**, 108312.
138 A. Tiwari, V. Singh, D. Mandal and T. C. Nagaiah, *J. Mater. Chem. A*, 2017, **5**, 20014–20023.
139 Q. Shi, F. Peng, S. Liao, H. Wang, H. Yu, Z. Liu, B. Zhang and D. Su, *J. Mater. Chem. A*, 2013, **1**, 14853.
140 K. Gong, F. Du, Z. Xia, M. Durstock and L. Dai, *Science*, 2009, **323**, 760–764.
141 S. Xin, Z. Liu, L. Ma, Y. Sun, C. Xiao, F. Li and Y. Du, *Nano Res.*, 2016, **9**, 3795–3811.
142 T. Wang, J. Zhuo, Y. Chen, K. Du, P. Papakonstantinou, Z. Zhu, Y. Shao and M. Li, *ChemCatChem*, 2014, **6**, 1877–1881.
143 L. Liao, J. Zhu, X. Bian, L. Zhu, M. D. Scanlon, H. H. Girault and B. Liu, *Adv. Funct. Mater.*, 2013, **23**, 5326–5333.
144 H. Li, C. Tsai, A. L. Koh, L. Cai, A. W. Contryman, A. H. Fragapane, J. Zhao, H. S. Han, H. C. Manoharan, F. Abild-Pedersen, J. K. Nørskov and X. Zheng, *Nat. Mater.*, 2016, **15**, 48–53.
145 L. Ma, H. Zhou, S. Xin, C. Xiao, F. Li and S. Ding, *Electrochim. Acta*, 2015, **178**, 767–777.
146 S. Kolagatla, P. Subramanian and A. Schechter, *ChemSusChem*, 2019, **12**, 2708–2714.
147 M. A. O'Connell, J. R. Lewis and A. J. Wain, *Chem. Commun.*, 2015, **51**, 10314–10317.
148 D. Yan, Y. Li, J. Huo, R. Chen, L. Dai and S. Wang, *Adv. Mater.*, 2017, **29**, 1606459.
149 A. Shen, Y. Zou, Q. Wang, R. A. W. Dryfe, X. Huang, S. Dou, L. Dai and S. Wang, *Angew. Chem.*, 2014, **126**, 10980–10984.
150 D. Perry, B. Paulose Nadappuram, D. Momotenko, P. D. Voyias, A. Page, G. Tripathi, B. G. Frenguelli and P. R. Unwin, *J. Am. Chem. Soc.*, 2016, **138**, 3152–3160.
151 L. Tao, M. Qiao, R. Jin, Y. Li, Z. Xiao, Y. Wang, N. Zhang, C. Xie, Q. He, D. Jiang, G. Yu, Y. Li and S. Wang, *Angew. Chem.*, 2019, **131**, 1031–1036.
152 M. Tahir, L. Pan, F. Idrees, X. Zhang, L. Wang, J.-J. Zou and Z. L. Wang, *Nano Energy*, 2017, **37**, 136–157.
153 Y. Liu, H. Cheng, M. Lyu, S. Fan, Q. Liu, W. Zhang, Y. Zhi, C. Wang, C. Xiao, S. Wei, B. Ye and Y. Xie, *J. Am. Chem. Soc.*, 2014, **136**, 15670–15675.
154 F. Song and X. Hu, *Nat. Commun.*, 2014, **5**, 4477.
155 H. Liang, F. Meng, M. Cabán-Acevedo, L. Li, A. Forticaux, L. Xiu, Z. Wang and S. Jin, *Nano Lett.*, 2015, **15**, 1421–1427.
156 N.-T. Suen, S.-F. Hung, Q. Quan, N. Zhang, Y.-J. Xu and H. M. Chen, *Chem. Soc. Rev.*, 2017, **46**, 337–365.
157 Y. Matsumoto and E. Sato, *Mater. Chem. Phys.*, 1986, **14**, 397–426.
158 B. Konkena, J. Masa, A. J. R. Botz, I. Sinev, W. Xia, J. Koßmann, R. Drautz, M. Muhler and W. Schuhmann, *ACS Catal.*, 2017, **7**, 229–237.
159 M. Gong, Y. Li, H. Wang, Y. Liang, J. Z. Wu, J. Zhou, J. Wang, T. Regier, F. Wei and H. Dai, *J. Am. Chem. Soc.*, 2013, **135**, 8452–8455.
160 M. W. Louie and A. T. Bell, *J. Am. Chem. Soc.*, 2013, **135**, 12329–12337.
161 A. Minguzzi, D. Battistel, J. Rodríguez-López, A. Vertova, S. Rondinini, A. J. Bard and S. Daniele, *J. Phys. Chem. C*, 2015, **119**, 2941–2947.
162 A. Minguzzi, M. A. Alpuche-Aviles, J. R. López, S. Rondinini and A. J. Bard, *Anal. Chem.*, 2008, **80**, 4055–4064.
163 F. Jiao and H. Frei, *Angew. Chem., Int. Ed.*, 2009, **48**, 1841–1844.
164 J. Y. Kim, H. S. Ahn and A. J. Bard, *Anal. Chem.*, 2018, **90**, 3045–3049.
165 J. M. Barforoush, T. E. Seuferling, D. T. Jantz, K. R. Song and K. C. Leonard, *ACS Appl. Energy Mater.*, 2018, **1**, 1415–1423.
166 N. Arroyo-Currás and A. J. Bard, *J. Phys. Chem. C*, 2015, **119**, 8147–8154.
167 M. Steimecke, G. Seiffarth and M. Bron, *Anal. Chem.*, 2017, **89**, 10679–10686.
168 S. Klaus, Y. Cai, M. W. Louie, L. Trotochaud and A. T. Bell, *J. Phys. Chem. C*, 2015, **119**, 7243–7254.
169 L. Trotochaud, S. L. Young, J. K. Ranney and S. W. Boettcher, *J. Am. Chem. Soc.*, 2014, **136**, 6744–6753.
170 M. Lu, S. Kharkwal, H. Y. Ng and S. F. Y. Li, *Biosens. Bioelectron.*, 2011, **26**, 4728–4732.
171 C. Zhang, N. Mahmood, H. Yin, F. Liu and Y. Hou, *Adv. Mater.*, 2013, **25**, 4932–4937.
172 J. Wu, H. W. Park, A. Yu, D. Higgins and Z. Chen, *J. Phys. Chem. C*, 2012, **116**, 9427–9432.
173 F. Song, L. Bai, A. Moysiadou, S. Lee, C. Hu, L. Liardet and X. Hu, *J. Am. Chem. Soc.*, 2018, **140**, 7748–7759.
174 C. W. B. Bezerra, L. Zhang, K. Lee, H. Liu, A. L. B. Marques, E. P. Marques, H. Wang and J. Zhang, *Electrochim. Acta*, 2008, **53**, 4937–4951.

© 2021 The Author(s). Published by the Royal Society of Chemistry

Open Access Article. Published on 19 November 2020. Downloaded on 4/20/2026 1:55:05 AM.
This article is licensed under a Creative Commons Attribution-NonCommercial 3.0 Unported Licence.

175 L. Yang, Y. Zhao, S. Chen, Q. Wu, X. Wang and Z. Hu, *Chin. J. Catal.*, 2013, **34**, 1986–1991.
176 D. Higgins, P. Zamani, A. Yu and Z. Chen, *Energy Environ. Sci.*, 2016, **9**, 357–390.
177 R. Jiang, S. on Tung, Z. Tang, L. Li, L. Ding, X. Xi, Y. Liu, L. Zhang and J. Zhang, *Energy Storage Mater.*, 2018, **12**, 260–276.
178 M. Shao, Q. Chang, J.-P. Dodelet and R. Chenitz, *Chem. Rev.*, 2016, **116**, 3594–3657.
179 M.-I. Jamesh and X. Sun, *J. Power Sources*, 2018, **400**, 31–68.
180 H.-F. Wang, C. Tang, B.-Q. Li and Q. Zhang, *Inorg. Chem. Front.*, 2018, **5**, 521–534.
181 J. Li and G. Zheng, *Adv. Sci.*, 2017, **4**, 1600380.
182 T. Reier, H. N. Nong, D. Teschner, R. Schlögl and P. Strasser, *Adv. Energy Mater.*, 2017, **7**, 1601275.
183 M. I. Jamesh, *J. Power Sources*, 2016, **333**, 213–236.
184 S. R. Narayan, A. Manohar and S. Mukerjee, *Interface Magazine*, 2015, **24**, 65–69.
185 M. Busch, N. B. Halck, U. I. Kramm, S. Siahrostami, P. Krtil and J. Rossmeisl, *Nano Energy*, 2016, **29**, 126–135.
186 G. Seiffarth, M. Steimecke, T. Walther, M. Kühhirt, S. Rümmler and M. Bron, *Electroanalysis*, 2016, **28**, 2335–2345.
187 S. Chakrabarty, A. Mukherjee, W.-N. Su and S. Basu, *Int. J. Hydrogen Energy*, 2019, **44**, 1565–1578.
188 L. Ma, H. Zhou, Y. Sun, S. Xin, C. Xiao, A. Kumatani, T. Matsue, P. Zhang, S. Ding and F. Li, *Electrochim. Acta*, 2017, **252**, 338–349.
189 S. Barwe, C. Andronescu, R. Engels, F. Conzuelo, S. Seisel, P. Wilde, Y.-T. Chen, J. Masa and W. Schuhmann, *Electrochim. Acta*, 2019, **297**, 1042–1051.
190 Y. Liao, K. Mustonen, S. Tulić, V. Skákalová, S. A. Khan, P. Laiho, Q. Zhang, C. Li, M. R. A. Monazam, J. Kotakoski, H. Lipsanen and E. I. Kauppinen, *ACS Nano*, 2019, **13**, 11522–11529.
191 A. Lasia, in *Handbook of Fuel Cells*, ed. W. Vielstich, A. Lamm, H. A. Gasteiger and H. Yokokawa, John Wiley & Sons, Ltd, Chichester, UK, 2010.
192 M. Gong, D.-Y. Wang, C.-C. Chen, B.-J. Hwang and H. Dai, *Nano Res.*, 2016, **9**, 28–46.
193 Z. W. Seh, J. Kibsgaard, C. F. Dickens, I. Chorkendorff, J. K. Nørskov and T. F. Jaramillo, *Science*, 2017, **355**, eaad4998.
194 J. Zhang, H. Li, P. Guo, H. Ma and X. S. Zhao, *J. Mater. Chem. A*, 2016, **4**, 8497–8511.
195 M. G. Walter, E. L. Warren, J. R. McKone, S. W. Boettcher, Q. Mi, E. A. Santori and N. S. Lewis, *Chem. Rev.*, 2010, **110**, 6446–6473.
196 S. Trasatti, *J. Electroanal. Chem. Interfacial Electrochem.*, 1972, **39**, 163–184.
197 J. L. Fernández and C. G. Zoski, *J. Phys. Chem. C*, 2018, **122**, 71–82.
198 G. Valenti, A. Boni, M. Melchionna, M. Cargnello, L. Nasi, G. Bertoni, R. J. Gorte, M. Marcaccio, S. Rapino, M. Bonchio, P. Fornasiero, M. Prato and F. Paolucci, *Nat. Commun.*, 2016, **7**, 13549.
199 Z. Wu, B. Fang, A. Bonakdarpour, A. Sun, D. P. Wilkinson and D. Wang, *Appl. Catal., B*, 2012, **125**, 59–66.
200 M. S. Faber, M. A. Lukowski, Q. Ding, N. S. Kaiser and S. Jin, *J. Phys. Chem. C*, 2014, **118**, 21347–21356.
201 P. D. Tran, T. V. Tran, M. Orio, S. Torelli, Q. D. Truong, K. Nayuki, Y. Sasaki, S. Y. Chiam, R. Yi, I. Honma, J. Barber and V. Artero, *Nat. Mater.*, 2016, **15**, 640–646.
202 D. Jasion, J. M. Barforoush, Q. Qiao, Y. Zhu, S. Ren and K. C. Leonard, *ACS Catal.*, 2015, **5**, 6653–6657.
203 X. Zou and Y. Zhang, *Chem. Soc. Rev.*, 2015, **44**, 5148–5180.
204 S. H. Salleh, S. Thomas, J. A. Yuwono, K. Venkatesan and N. Birbilis, *Electrochim. Acta*, 2015, **161**, 144–152.
205 T. Zhang, Z. Tao and J. Chen, *Mater. Horiz.*, 2014, **1**, 196–206.
206 A. Kundu, J. H. Gil, J. H. Jang, H. R. Lee, C. R. Jung, B. S. Ku and K. S. Chae, *Int. J. Hydrogen Energy*, 2010, **35**, 10827–10832.
207 A. Nidola and R. Schira, *Int. J. Hydrogen Energy*, 1986, **11**, 449–454.
208 D. Merki and X. Hu, *Energy Environ. Sci.*, 2011, **4**, 3878.
209 B. Hinnemann, P. G. Moses, J. Bonde, K. P. Jørgensen, J. H. Nielsen, S. Horch, I. Chorkendorff and J. K. Nørskov, *J. Am. Chem. Soc.*, 2005, **127**, 5308–5309.
210 T. F. Jaramillo, K. P. Jorgensen, J. Bonde, J. H. Nielsen, S. Horch and I. Chorkendorff, *Science*, 2007, **317**, 100–102.
211 H. Li, M. Du, M. J. Mleczko, A. L. Koh, Y. Nishi, E. Pop, A. J. Bard and X. Zheng, *J. Am. Chem. Soc.*, 2016, **138**, 5123–5129.
212 C. Ataca and S. Ciraci, *Phys. Rev. B*, 2012, **85**, 195410.
213 H. Li, K. Yu, C. Li, Z. Tang, B. Guo, X. Lei, H. Fu and Z. Zhu, *Sci. Rep.*, 2015, **5**, 18730.
214 S. Kumar, P. K. Sahoo and A. K. Satpati, *ACS Omega*, 2017, **2**, 7532–7545.
215 X. Gao, Y. Chen, T. Sun, J. Huang, W. Zhang, Q. Wang and R. Cao, *Energy Environ. Sci.*, 2020, **13**, 174–182.
216 J. Jedraszko, W. Adamiak, W. Nogala, H. H. Girault and M. Opallo, *J. Electroanal. Chem.*, 2018, **819**, 101–106.
217 C. L. Bentley and P. R. Unwin, *Faraday Discuss.*, 2018, **210**, 365–379.
218 M. Choi, N. P. Siepser, S. Jeong, Y. Wang, G. Jagdale, X. Ye and L. A. Baker, *Nano Lett.*, 2020, **20**, 1233–1239.
219 L. Britnell, R. V. Gorbachev, R. Jalil, B. D. Belle, F. Schedin, M. I. Katsnelson, L. Eaves, S. V. Morozov, A. S. Mayorov, N. M. R. Peres, A. H. Castro Neto, J. Leist, A. K. Geim, L. A. Ponomarenko and K. S. Novoselov, *Nano Lett.*, 2012, **12**, 1707–1710.
220 M. Gao, A. Lyalin and T. Taketsugu, *Int. J. Quantum Chem.*, 2013, **113**, 443–452.
221 D.-Q. Liu, B. Tao, H.-C. Ruan, C. L. Bentley and P. R. Unwin, *Chem. Commun.*, 2019, **55**, 628–631.
222 X. Duan, J. Xu, Z. Wei, J. Ma, S. Guo, S. Wang, H. Liu and S. Dou, *Adv. Mater.*, 2017, **29**, 1701784.
223 C. Costentin, M. Robert and J.-M. Savéant, *Chem. Soc. Rev.*, 2013, **42**, 2423–2436.
224 G. A. Olah, A. Goeppert and G. K. S. Prakash, *J. Org. Chem.*, 2009, **74**, 487–498.

Open Access Article. Published on 19 November 2020. Downloaded on 4/20/2026 1:55:05 AM.
This article is licensed under a Creative Commons Attribution-NonCommercial 3.0 Unported Licence.

225 W.-H. Wang, Y. Himeda, J. T. Muckerman, G. F. Manbeck and E. Fujita, *Chem. Rev.*, 2015, **115**, 12936–12973.
226 J. Zhang, W. J. Pietro and A. B. P. Lever, *J. Electroanal. Chem.*, 1996, **403**, 93–100.
227 F. Zhang and A. C. Co, *J. Electrochem. Soc.*, 2020, **167**, 046517.
228 A. Wadas, I. A. Rutkowska, M. Bartel, S. Zoladek, K. Rajeshwar and P. J. Kulesza, *Russ. J. Electrochem.*, 2017, **53**, 1194–1203.
229 N. Sreekanth and K. L. Phani, *Chem. Commun.*, 2014, **50**, 11143–11146.
230 N. Sreekanth, M. A. Nazrulla, T. V. Vineesh, K. Sailaja and K. L. Phani, *Chem. Commun.*, 2015, **51**, 16061–16064.
231 Y. Hori, in *Modern Aspects of Electrochemistry*, ed. C. G. Vayenas, R. E. White and M. E. Gamboa-Aldeco, Springer New York, New York, NY, 2008, vol. 42, pp. 89–189.
232 A. A. Arrocha-Arcos, R. Cervantes-Alcalá, G. A. Huerta-Miranda and M. Miranda-Hernández, *Electrochim. Acta*, 2017, **246**, 1082–1087.
233 C. Amatore and J. M. Saveant, *J. Am. Chem. Soc.*, 1981, **103**, 5021–5023.
234 A. Verdaguer-Casadevall, C. W. Li, T. P. Johansson, S. B. Scott, J. T. McKeown, M. Kumar, I. E. L. Stephens, M. W. Kanan and I. Chorkendorff, *J. Am. Chem. Soc.*, 2015, **137**, 9808–9811.
235 C. W. Li, J. Ciston and M. W. Kanan, *Nature*, 2014, **508**, 504–507.
236 R. G. Mariano, K. McKelvey, H. S. White and M. W. Kanan, *Science*, 2017, **358**, 1187–1192.
237 S. C. S. Lai, P. V. Dudin, J. V. Macpherson and P. R. Unwin, *J. Am. Chem. Soc.*, 2011, **133**, 10744–10747.

© 2021 The Author(s). Published by the Royal Society of Chemistry